https://doi.org/10.5194/egusphere-2026-1536
Preprint. Discussion started: 11 May 2026

Combined luminescence dating and ice-flow modelling to track Holocene sediment transport and storage in the Mer de Glace catchment, French Alps

Léa Rodari[1,2], Audrey Margirier[1,3], Ann V. Rowan[4], Christoph Schmidt[1], Remy Veness[5], Charlotte S. Curry[6], Alex C. Scoffield[7], Christiaan R. Diemont[6], Faye Perchanok[1], Guillaume Jouvet[1], Vivi Pedersen[8], Derek Fabel[9], Georgina E. King[1]

[1]Institute of Earth Surface Dynamics, University of Lausanne, Lausanne, Switzerland
[2]Department of Geography and Social Anthropology, Norwegian University of Science and Technology, Trondheim, Norway
[3]Univ. Grenoble Alpes, Univ. Savoie Mont Blanc, CNRS, Univ. Gustave Eiffel, ISTERRE 38000 Grenoble, France
[4]Department of Earth Science, University of Bergen and Bjerknes Centre for Climate Research, Bergen, Norway
[5]Department of the Natural and Built Environment, Sheffield Hallam University, Sheffield, UK
[6]School of Geography & Planning, University of Sheffield, Sheffield, UK
[7]School of Geography and water@leeds, University of Leeds, Leeds, UK
[8]Department of Geoscience, Aarhus University, Denmark
[9]Scottish Universities Environmental Research Centre (SUERC), the University of Glasgow, UK

Correspondence to: Léa Rodari (lea.rodari@ntnu.no)

https://doi.org/10.5194/egusphere-2026-1536
Preprint. Discussion started: 11 May 2026

Abstract

The storage and release of sediment from glacierised catchments is an important process in mountain landscape evolution, and yet sediment transport pathways and residence times within glaciers remain poorly constrained. We quantified headwall erosion rates and englacial sediment transport and storage times in the Mer de Glace catchment in the Mont Blanc massif, French Alps, during deglaciation through the Holocene (11.7 ka to present). Englacial sediment transport and storage times were constrained using luminescence rock surface burial ages of granitic clasts sampled along the central flow line of the Mer de Glace ablation area. We also used luminescence rock surface exposure dating and terrestrial cosmogenic nuclide (^{10}Be) measurements to constrain headwall erosion rates for this catchment. These headwall erosion and sediment transport data were compared with simulated erosion, sediment trajectories and transport rates derived from the glacier model iSOSIA. Measured headwall erosion rates were ~0.1–5 mm a^{-1} and are consistent with other estimates from the Mont Blanc massif. Luminescence rock surface burial ages ranged from ~0.6 to ~6.7 ka and clustered into distinct age populations at ~0.8 ka, ~1.5 ka, ~2.2 ka, and ~6.7 ka. The youngest age population is consistent with continuous englacial transport times predicted by the glacier modelling and observations of present-day glacier surface velocity, whereas the older age clusters indicate prolonged sediment storage within the catchment. Comparison of our results with results from Miage Glacier, Italian Alps, shows that long-term sediment storage with durations exceeding 1 ka is common in steep alpine glacierised catchments, despite high erosion rates and active ice flow. Luminescence burial ages indicate that sediment can be stored during periods of glacier minima, then released during more active phases. Glacierised catchments therefore act as millennial-scale sediment reservoirs, introducing time lags between sediment production and downstream transport, that modulate climatic signals recorded in proglacial stratigraphy during deglaciation.

1 Introduction

The storage and release of sediment from deglaciating catchments is an important contribution to the evolution of mountain landscapes, but is relatively poorly understood because glacial sediment transport processes are difficult to observe, occurring over time scales ranging from the catchment response to interannual variability (days, weeks, and months) to the time scales of glacier advance and recession (hundreds to thousands of years) (Scherler et al.,

https://doi.org/10.5194/egusphere-2026-1536
Preprint. Discussion started: 11 May 2026

2011; Delaney et al., 2026). Understanding glacial sediment transport is important as the presence of sediment at the glacier bed substantially modifies the evolution of glaciers away from the assumed behaviour of glaciers that flow over bedrock (Lane et al., 2017). Sediment produced by bedrock erosion on the headwalls above the glacier surface is typically transported englacially and supraglacially, while sediment produced by erosion at the glacier bed generally remains subglacial (Hallet et al., 1996; Rowan et al., 2015). Supraglacial debris accumulation changes surface mass balance and the response of glaciers to climate change (Deline et al., 2015; Fyffe et al., 2020; Rowan et al., 2015, 2021) and the feedbacks that occur due to the transport of sediment affects the formation of ice-marginal moraines and the formation of the geological record of glaciation (Anderson et al., 2012; Rowan et al., 2022). However, little is known about the rates and relative contributions of these different sediment transport processes to the total sediment flux through and from a glacierised catchment.

Supraglacial debris is present on approximately 7% of mountain glaciers worldwide, and the glacierised area covered with debris is expected to increase in the future with ongoing ice mass loss (Herreid & Pellicciotti, 2020). Rock debris (sediment) falling from the surrounding headwalls either as individual clasts or larger landslides onto the accumulation area of a glacier is incorporated into the ice before being transported englacially to the ablation area where it is exhumed to the glacier surface, and sediment can also enter englacial transport through deposition into crevasses and moulins which can remain open in the ablation zone (Anderson, 2000). Debris deposited on the glacier surface in the ablation area is predominantly transported supraglacially to the ice margins (Kirkbride & Deline, 2013; Rowan et al., 2015; Anderson and Anderson, 2018), whereas debris produced by subglacial erosion in the lower part of the ice column can be incorporated into the ice by regelation from the bed (Iverson, 1993; Alley et al., 1997; Hambrey et al., 1999). Sediment is transported passively within the glacier following internal dynamics of ice and at the bed (Goodsell et al., 2005; Jennings & Hambrey, 2021), and englacially and subglacially by water flow through englacial or subglacial channels (Alley et al., 1997; Kirkbride, 2002). Englacial debris transport is influenced by sediment input location, englacial structure (e.g. fractures or foliation), ice internal deformation (Goodsell et al., 2005; Jennings & Hambrey, 2021) and the thermal regime and surface mass balance of the glacier (Kirkbride & Deline, 2013). Englacial sediment transport therefore affects glacial evolution because the accumulation of supraglacial debris modifies surface ablation, both by reducing albedo and by insulating the underlying ice (Nicholson et al., 2021). Glacier change in response to climate change affects the delivery of sediment to the catchment from headwalls. During periods of deglaciation, the reduction in ice volume destabilises hillslopes and may increase bedrock erosion if sediment is exported rather than covering the hillslopes (Scherler,

https://doi.org/10.5194/egusphere-2026-1536
Preprint. Discussion started: 11 May 2026

2014). As ice flow decreases, debris exhumed to the glacier surface is stored supraglacially and the debris-covered area expands upglacier (Rowan et al., 2015). In contrast, during periods of glacier expansion, active ice flow is able to efficiently transport sediment and a glacier is less likely to develop an extensive debris cover, although medial and lateral moraines can form (Anderson, 2000; Kirkbride & Deline, 2013; Deline et al., 2015; Nicholson et al., 2021).

The processes by which glaciers transport ice and sediment are difficult to observe. Satellite imagery allows surface features such as supraglacial boulders to be tracked to map glacier surface velocities (e.g., Millan et al., 2022), but ice flow at depth is much more difficult to observe directly, and few data exist (e.g., Jennings & Hambrey, 2021). For example, the observed trajectories of unfortunate mountaineers' bodies found at the surface of Aletsch Glacier, Switzerland, were used to constrain a glacier model to determine their original burial site 86 years previously (Jouvet & Funk, 2014). Radionuclides have also been used as an englacial tracer to understand the trajectories of particles moving through the Gauligletscher (Jouvet et al., 2020). Such anthropogenic tracers are useful for measuring current or recent rates of ice flow, but cannot constrain longer-term glacial transport of sediment, which is expected to occur across a wide range of timescales of up to 10^3–10^4 years in response to climate change (Margirier et al., 2025). The recent development of geochronological and numerical modelling methods to measure the duration of sediment transport through glaciers allows these processes to be explored over timescales of deglaciation: Analysis of the exposure history of supraglacial debris using the cosmogenic nuclide ^{10}Be combined with a Lagrangian ice-flow model explored temporal variability in paraglacial erosion rates at Chhota Shigri Glacier, India (Scherler & Egholm, 2020), and the same glacier modelling approach combined with low-temperature thermochronological data revealed spatial variability in headwall erosion rates at Tiedemann Glacier in British Columbia, Canada (Bernard et al., 2020).

Luminescence dating of rock surfaces (Richards, 1992) offers a valuable method for dating geomorphic processes in glacierised catchments at a higher temporal resolution than is possible with other geochronological methods (e.g., King et al., 2019). Luminescence rock-surface burial dating (Sohbati et al., 2012) has been used to measure the burial or transport duration of glaciofluvial cobbles (Jenkins et al., 2018), moraine deposits (Rades et al., 2018), and englacial clasts (Margirier et al., 2025). Furthermore, luminescence rock-surface exposure-age dating coupled with cosmogenic-nuclide exposure-age dating can provide estimates of headwall erosion rates for glacial catchments (e.g. Lehmann et al., 2019b). The aim of this study is to determine transport rates and trajectories of

https://doi.org/10.5194/egusphere-2026-1536
Preprint. Discussion started: 11 May 2026

sediment produced by headwall erosion through a large alpine glacier over timescales representative of glacier evolution during a period of ongoing climate change and deglaciation. This study applies recently developed luminescence exposure-age dating and rock surface burial dating methods (Lehmann et al., 2019b; Margirier et al., 2025) to constrain Holocene rates of headwall erosion and englacial sediment transport at Mer de Glace in the Mont Blanc massif of the French Alps (Fig. 1). To determine the glacial transport trajectories represented by the sampled sediment clasts, we simulated the entrainment and transport of englacial particles through this glacier using a Lagrangian glacier model iSOSIA (Scherler & Egholm, 2020; Margirier et al., 2025) and compare these results with the sediment transport durations derived from the luminescence measurements.

2 Study site

Mer de Glace (RGI60-11.03643; RGI Consortium, 2017) is a large valley glacier in the Mont Blanc massif, French Alps (Fig. 1) which has been the subject of numerous glaciological studies and historical observations of glacier change over the last 150 years. Mer de Glace is a complex glacier composed of several tributary glaciers; Géant Glacier, Périades Glacier, Tacul Glacier, and Leschaux Glacier and the disconnected former tributary Talèfre Glacier (Fig. 1A). The entire glacier system (excluding Talèfre Glacier) has a length of 11.5 km and an area of ~28 km^2 (GLACIOCLIM, 2019), spanning an elevation range from 1529 m to 4025 m above sea level (a.s.l.) in 2022 (GLIMS Consortium, 2005). Mer de Glace is a clean-ice glacier, with narrow debris-rich bands forming medial moraines where tributary glaciers converge and lateral moraines occurring between the ice margin and the steep hillslopes that constrain the ablation area, which hosts striking band ogives below the Tacul icefall (Vincent et al., 2018). The Mer de Glace catchment is mainly underlain by granitic lithologies, apart from in the northern part of the Echellets hillslope where the bedrock is orthogneiss (von Raumer & Bussy, 2004). The catchment has high-relief with hillslopes exceeding 28° and fractured bedrock that promotes frequent mass movements (e.g., rock falls, landslides, snow avalanches) (Deline, 2009).

Changes of glacier surface velocity, length, and ice thickness at Mer de Glace have been measured since 1878 (e.g., Reid, 1902; Lliboutry & Reynaud, 1981; Vincent et al., 2019) and these observations provided a detailed description of the present state of this glacier. The mean ice thickness in the accumulation area at the Col du Midi was measured as about 180 m in 1975 (Vallon et al., 1976). The mean ice thickness in the ablation area was

https://doi.org/10.5194/egusphere-2026-1536
Preprint. Discussion started: 11 May 2026

measured as about 360 m at the Tacul-Leschaux Glacier confluence in 2015 (Peyaud et al., 2020) and about 80 m at the Montenvers profile in 2009 (Vincent, 2010). The glacier is shrinking and the ablation area is becoming increasingly debris-covered (Berthier & Vincent, 2012). Mer de Glace has experienced an acceleration in ice loss over the last three decades (GLACIOCLIM, 2019; Vincent et al., 2014), with ~50 m (32 %) of ice thickness loss (Vincent et al., 2019) and 1.53 km of terminus recession between 1878–2022. Satellite observations indicate that the rate of surface elevation change was –4.1 ± 1.7 m a^{-1} between 2000–2003, which is four times higher than the rate of –1.0 ± 0.4 m a^{-1} observed between 1979–1994 CE (Common Era; Berthier et al., 2004). Glacier surface velocity slowed across the entire ablation area by 51–53 % between 1985–2005, accompanied by thinning of 17–23% and a reduction in ice flux of 60% (Berthier & Vincent, 2012).

Historical photographs from 1902 show that the surface of the central flowline of the glacier was generally free of supraglacial debris when the terminus of Mer de Glace extended into the Chamonix Valley, apart from the thin layers of dust that covered the Séracs du Géant icefall and the prominent ogives in the upper ablation area, while the flow unit on the true right that joins Mer de Glace from Glacier de Leschaux was at least partially debris-covered with several merging medial moraines in the lower ablation area (Reid, 1902). Historical maps of Mer de Glace from the 1800s show that the supraglacial debris cover on the Glacier de Leschaux flow unit started to expand as four medial moraines formed and merged around 1820–1830 during the climatic transition at the end of the Little Ice Age (LIA), and a patchy debris layer started to develop at the terminus becoming more continuous from 1840 onwards (Deline, 2005). Since the end of the 19th Century, the true right part of the lower ablation area was a single debris-covered unit of 1.2 km^2 (35–40% of the tongue area) called the “black vein” (Deline, 2005). Expansion and reduction of supraglacial debris cover on Mer de Glace has occurred several times during the Holocene, linked to periods of advance and recession (Deline, 2005).

https://doi.org/10.5194/egusphere-2026-1536
Preprint. Discussion started: 11 May 2026

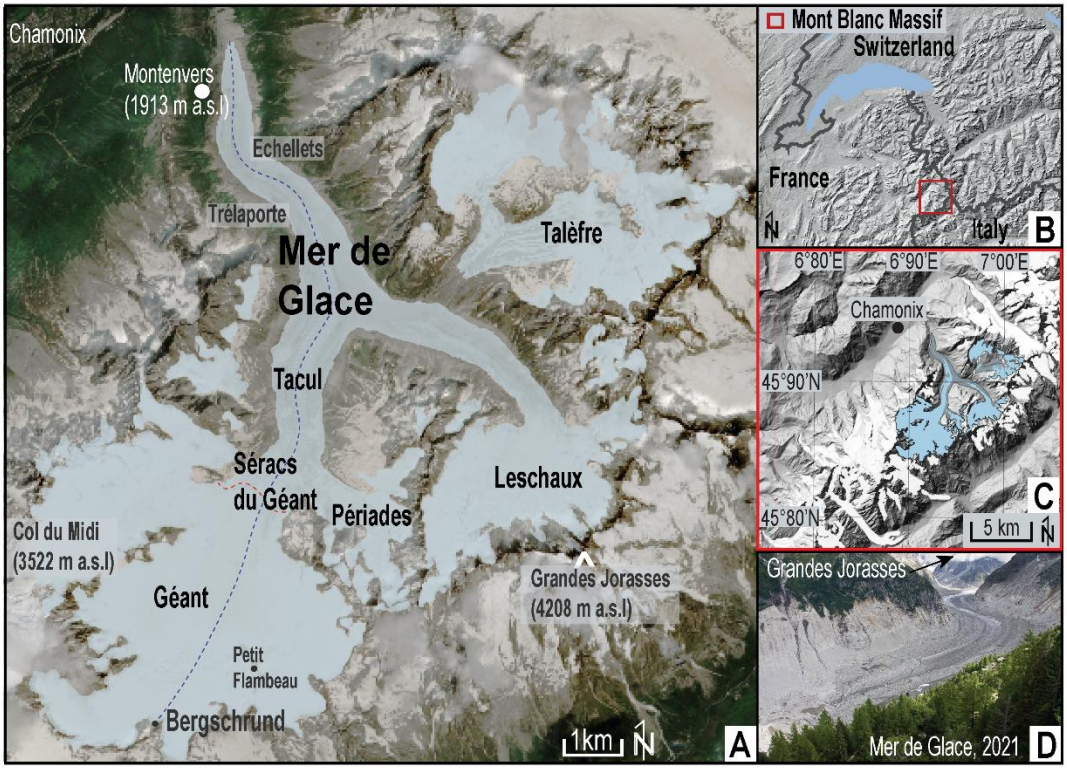

Figure 1. A) Map of Mer de Glace in the French Alps image from the Copernicus Sentinel-2 (28.06.2023). Dotted lines represent the length of the glacier from the bergschrund to the glacier front (blue) and the estimated location of the ELA (orange) based on the 2022 data (GLIMS Consortium, 2005). B) Location of the Mont-Blanc Massif within the Western European Alps. The background DEM is SwissALTIRegio 2023 (Swisstopo, Tarquini et al., 2023). C) The Mont-Blanc massif at a regional scale with the glaciated area from GLIMS Consortium, (2005), background DEM is swissALTIRegio 2023 (Swisstopo, Tarquini et al., 2023). D) Photograph of Mer de Glace taken from Montenvers in August 2021.

2.1 Sampling strategy

Samples were collected to constrain both headwall erosion rates and rates of englacial particle transport through the Mer de Glace catchment. Headwall erosion rates were measured following the approach of Lehmann et al., (2019a; 2019b), using paired ^{10}Be terrestrial cosmogenic nuclide (TCN) and luminescence rock surface exposure dating (RSED). Whereas the ^{10}Be starts to accumulate in quartz-bearing rocks once the ice thickness is less than 30 cm, the luminescence signal is only progressively reset following exposure after complete removal of ice. Luminescence signals change over mm-scale depths and are thus highly sensitive to erosion and can be used to adjust TCN data for rock surface erosion effects, allowing a precise estimation of erosion rate.

https://doi.org/10.5194/egusphere-2026-1536
Preprint. Discussion started: 11 May 2026

For measurement of the headwall erosion rates, four rock samples were collected using a hammer and chisel for paired luminescence RSED and TCN dating from the face of the Petit Flambeau which has a SSW aspect in the accumulation area (Fig. 1A, Table S1). A known-age sample was needed to calibrate the parameters used in the luminescence RSED calculation (e.g. Lehmann et al., 2018b), and consequently each sample location was resampled approximately one year later.

For measurement of englacial transport rates, a total of 27 granitic clasts with diameters greater than 5 cm were collected in the ablation area of Mer de Glace for luminescence rock surface burial dating (RSBD). Samples were collected along a transect following the central flow line (Fig. 1A) away from the ice margins to prevent the sampling of rock clasts that have been re-entrained from supraglacial, subglacial, or lateral moraine deposits. Selected samples were embedded in steep ice faces below the glacier surface with a slope greater than 60° with some samples taken from ice cliffs carved by supraglacial streams and others from relict moulins.

3 Methods

3.1 Luminescence dating

Sample preparation was completed under subdued red-light conditions at the University of Lausanne, Switzerland using established methods (e.g. Lehmann et al., 2019b; Margirier et al., 2025). For each RSED sample, two cores were extracted from the exposed rock surface, whereas for luminescence rock surface burial dating (RSBD) one core was taken from each buried (non-exposed) rock-surface. Cores were cut into ~1 mm thick slices and for the RSBD samples, a portion of each sample was retained to constrain the environmental dose rate. Luminescence signals were measured using a single Risø TL/OSL DA-20 reader equipped with a Sr^{90}/Yr^{90} beta-source and a DASH (Lappe et al., 2015). Measurements followed the protocol of Elkadi et al., (2021) (Table S3) and included infrared stimulation at 50°C ($IRSL_{50}$) and at 225°C ($IRSL_{225}$), and blue stimulation at 125°C (OSL_{125}). Fragments of each rock slice were placed in stainless-steel cups for measurement. Measurements that yielded recycling ratios of <10 % were retained.

Luminescence bleaching profiles were fitted with a general-order kinetic model (Biswas et al., 2023; Freiesleben, et al., 2023a; 2023b; Pathan et al., 2024). For RSED, the luminescence detrapping probability, $\sigma\varphi_0$ (s^{-1}), the light attenuation coefficient, μ (mm^{-1}), and the order of kinetics, b, were obtained by fitting the luminescence

https://doi.org/10.5194/egusphere-2026-1536
Preprint. Discussion started: 11 May 2026

data of four calibration samples (Supplementary Material Section 3.4). We evaluated the reliability of this approach following Lehmann et al., (2018), whereby parameters were solved for using different combinations of samples (Supplementary Material Section 3.4).

Luminescence RSBD signal bleaching profiles were evaluated using a plateau test (Freiesleben, et al., 2015; Rades et al., 2018), whereby a predicted profile from bleaching only (exposure) is contrasted with the measured burial profile. If ≥2 discs of a sample yielded $IRSL_{50}$ luminescence signals that exhibited a >5% difference from the predicted bleaching only profile, the core was retained and equivalent dose (D_e) values were measured using a single aliquot regenerative dose (SAR) protocol (Murray & Wintle, 2000; Wallinga et al., 2000). Anomalous fading was measured for each sample following Auclair et al., (2003), and ages of samples with *g*-values >1%/decade were fading corrected. Data quality was confirmed using a dose recovery test.

Environmental dose rates were calculated using the conversion factors of Guérin et al., (2011), the alpha attenuation factors of Brennan et al., (1991), the beta etch attenuation factor of Bell, (1979) and an *a*-value of 0.15±0.05 (Balescu & Lamothe, 1994). The internal water content was fixed at 0.4±0.4% for all samples based on measured values (Table S6). As our samples were collected in the ice, the external radiation dose rate from the surrounding matrix was assumed to be zero, except for the cosmic dose rate that was calculated assuming a burial depth of 100 m, corresponding to half of the average glacier thickness (Vallon et al., 1976; Peyaud et al., 2020; Vincent, 2010). Although this assumption is not representative for all the samples, their trajectories in the ice are unknown and a change in thickness of 100 m has no significant impact on the age results. An internal K content of 12.5±0.5 % was included for the $IRSL_{50}$ and $IRSL_{225}$ signals that are assumed to originate from K-feldspar minerals (Huntley & Baril, 1997). K-feldspar and quartz grain sizes were estimated from one rock slice of each sample using optical microscopy and range from 100 to 2000 µm, with the largest grain size population being between 700 and 1100 µm. Following the approach of Freiesleben et al., (2015) the average of the larger grain size population was used for the age calculation, i.e. 850 µm to 950 µm. As our samples have diameters of 5-27 cm and their surrounding environment was ice, it was necessary to scale the gamma and beta dose rate using the calc_CobbleDoseRate() function (Riedesel & Autzen, 2020) in the R Luminescence package (Kreutzer et al., 2012, 2017). The output data from this function was input into DRAC v1.2 (Durcan et al., 2015) for the final dose rate calculation (Table S7).

RSBD ages were calculated for slices that fulfilled the plateau test and acceptance criteria outlined above. Once the ages were fading corrected, rock slice fragments from an individual sample that gave an age >1σ different

https://doi.org/10.5194/egusphere-2026-1536
Preprint. Discussion started: 11 May 2026

to the average of all the rock fragments from the plateau were considered outliers and removed (Supplementary Materials Section 3.5). If a sample contained only two rock fragments on the plateau and the ages were not consistent within uncertainty, the fragment with the lower age was retained. When several cores were taken from the same clast, the mean age of the dated cores was retained. The $IRSL_{50}$ signal yielded the most accepted data, consequently for interpretation of the glaciological processes only the mean $IRSL_{50}$ ages, calculated excluding outliers, are discussed (See Supplementary Materials for the complete dataset).

3.2 Cosmogenic nuclide exposure-age dating

Headwall bedrock samples for ^{10}Be dating were prepared and measured at the Scottish Universities Environmental Research Centre AMS facility, East Kilbride, UK. Rock samples were crushed and purified quartz extracted using standard methods (see Supplemental Material Section 2 for more detail of ^{10}Be sample preparation and measurement). Ages and erosion rates were calculated using the CREp calculator (Martin et al., 2017), using the LSD scaling scheme (Lifton et al., 2008), with the ERA-40 atmospheric model (Uppala et al., 2005), the LSD framework geomagnetic record (Laj et al., 2004; Korte et al., 2009; Ziegler et al., 2011; Lifton et al., 2014) and a local production rate from the Chironico landslide (Claude et al., 2014). Topographic shielding was calculated using the strike-dip of the rock surface and skyline measurements made in the field. Rock density was assumed to be 2.55 g cm^{-3} (Lehmann et al., 2019b). We did not apply a snow-cover correction because the Petit Flambeau headwall has a near-vertical slope that is unlikely to hold any significant cover of snow.

3.3 Inverse modelling of headwall erosion rates

The RSED data were inverted together with their paired ^{10}Be data to obtain the erosion history of each sample following Lehmann et al., (2019a; 2019b). We assumed that erosion rates ($\dot{\varepsilon}$) evolved as a step function from $\dot{\varepsilon}$= 0 to $\dot{\varepsilon} > 0$ at time t_s (Lehmann et al., 2019a; 2019b). A vector of $\dot{\varepsilon}$ and t_s values was generated, from which corrected exposure ages t_c were computed that satisfy both the RSED and TCN apparent ages. Erosion rates and durations inconsistent with the observed ^{10}Be concentrations (Lal, 1991) were excluded from the parameter search. We tested 10^5 pairs of $\dot{\varepsilon}$ and t_s (between 10^{-6} mm a^{-1} and 10 mm a^{-1} and t_s between 1 and 1000 years), which encompasses the range of TCN apparent ages (Table 1). An erosion rate of $<10^{-6}$ mm a^{-1} is considered to represent negligible erosion and to be beyond the resolution of the RSED and TCN methods.

https://doi.org/10.5194/egusphere-2026-1536
Preprint. Discussion started: 11 May 2026

3.4 Glacier modelling of sediment transport through Mer de Glace

3.4.1 Glacier model description

The glacial landscape evolution model iSOSIA (Egholm et al., 2011) was used to simulate the flow of Mer de Glace as well as the production, storage, and transport of sediment through the entire hydrological catchment. iSOSIA is a higher-order glacier model that simulates ice flow through high-relief topography in combination with erosion, transport, and deposition of sediment (Rowan et al., 2015; Scherler & Egholm, 2020). The model version used here includes a Lagrangian scheme that simulates the trajectory of individual sediment particles as points in time through the 3-D model domain (Scherler & Egholm, 2020). This approach allows the location and properties of each englacial particle (e.g., the source location, the age of production, the duration of time in transport on hillslopes, englacially, or subglacially) to be tracked through the simulation. Sediment particles can be deposited at the ice margin and stored as moraine before being re-entrained into glacial transport as the glacier extent and dynamics evolve.

Hillslopes steeper than the critical threshold (28°) were eroded to produce sediment that could then be entrained into glacial transport. Sediment produced by hillslope erosion was transported from the catchment headwalls using a non-linear hillslope flux model that relates sediment flux to topographic slope (Roering et al., 1999):

$$q_s = \frac{\mathrm{K}\,\nabla \mathrm{b}}{1-(\frac{|\nabla b|}{S_c})^2} \qquad \text{Eq(2)}$$

where q_s is hillslope sediment flux, ∇b is the tangent of the hillslope gradient (in radians), S_c is the critical slope, and the diffusivity constant, K, represents linear diffusion over time. Sediment flux increases in a near-linear fashion at low hillslope gradients and more rapidly as the gradient approaches the critical value (S_c); a positive value for q_s indicates the sediment flux from a cell and q_s is infinite when the local hillslope gradient (b) equals S_c, which is consistent with the concept of threshold hillslopes (Roering et al., 1999). Sediment storage and transport across the non-glacierised part of the catchment was simulated on the Eulerian grid, whereby sediment within the glacierised part was represented as a thickness in each grid cell until the sediment entered glacial transport. Sediment in englacial transport was tracked using a Lagrangian approach with 10^9 particles, whereby when sediment was in contact with ice a particle formed to represent the entrained material and was tracked through the

https://doi.org/10.5194/egusphere-2026-1536
Preprint. Discussion started: 11 May 2026

glacier until deposition. When particles were deposited from the glacier, the sediment they represented was returned to the grid cell that last contained the particle.

275

3.4.2 Mass balance

A temperature-index model with an elevation-dependent calculation of snow accumulation and an empirical value for ice ablation due to positive air temperatures (Equation 1) was used to calculate the mass balance of the present-day glacier. A uniform value for precipitation of 1 m a^{-1} was partitioned into snowfall based on the elevation-
280 dependent air temperature for each model time step. The critical temperature for rain–snow partitioning was set to 0°C. Accumulation was the result of the total snowfall in each cell and redistribution of the accumulated snowpack by avalanching from surfaces steeper than 28°, following a steepest descent path to redistribute mass across the hillslopes and glacier surfaces. Clean-ice ablation (*M;* in mm) was calculated using a degree-day factor approach (Hock, 2003):

285

$$\sum_{i=1}^{n} M = DDF \sum_{i=1}^{n} T^{+} \Delta t \qquad \text{Eq. (1)}$$

where air temperature (T) over time (t) was represented by a sinusoid around the mean annual air temperature at sea level with a seasonal amplitude of 6°C distributed across the model domain using a lapse rate of –6.0 °C km^{-1}.
290 The degree day factor for ice of 2.0 mm water equivalent (w.e.) per day per °C was chosen to fit the simulated glacier to the observed present-day ice extent. The mass balance variables used here followed those used for simulation of neighbouring Miage Glacier, Italy, in the Mt. Blanc massif by Margirier et al. (2025). Mer de Glace would have been confluent with other glaciers in the Chamonix Valley during the Younger Dryas, so to avoid simulating the entire region, mass balance was set to zero at the lower boundaries of the model domain.

295

3.4.3 Glacier model parameterisation and sensitivity testing

The subglacial model domain was defined to include the entire hydrological catchment of Mer de Glace and the glacier extent at the start of the Holocene using the 30-m ASTER GDEM version 2 (2011) from which the estimated
300 present-day ice thickness was subtracted (Farinotti et al., 2019) for all glaciers in the catchment with an area >1 km^2. The model domain was then resampled to a grid spacing of 100 m to optimise model stability and efficiency

https://doi.org/10.5194/egusphere-2026-1536
Preprint. Discussion started: 11 May 2026

giving a grid of 150 x 150 cells. The model time step varied according to the stability of the ice-flow calculations up to a maximum of 0.1 years. Values for the headwall erosion rate of between 0.001 m a^{-1} and 0.01 m a^{-1} were tested to represent the range of possible hillslope erosion rates for the Mer de Glace catchment derived from the headwall erosion rate measurements at the Petit Flambeau and existing literature (see Section 3.3).

Sensitivity tests were carried out to determine the most appropriate values for the model domain grid spacing, critical slope, hillslope erosion rate, precipitation rate, and degree-day factor, to use to define present-day surface mass balance constrained and evaluated against the current glacier geometry, including the position of medial moraines and the former ice-margin extent indicated by moraines dating from the Little Ice Age advance into the Chamonix Valley (Lüthi, 2014), and remote sensing observations of present-day ice thickness, velocity, and mass balance (Berthier & Vincent, 2012; Peyaud et al., 2020). The simulations were repeated to test the impact of the reduction in sub-debris melt beneath thick (>0.1 m) supraglacial debris on glacier evolution, using a reciprocal function that scaled clean-ice ablation with debris thickness (Rowan et al., 2021).

3.4.4 Climate forcing through deglaciation

To simulate the trajectories of the clasts collected in the ablation area of Mer de Glace today, the numerical model experiments encompassed the evolution of Mer de Glace through the deglaciation from the Younger Dryas and the Holocene period (11.7 ka to present). Immediately prior to the Holocene, Mer de Glace was more extensive than at present during the Younger Dryas maximum at 12.2 ± 1.0 ka (the Egesen stadial) that ended at 11.3 ± 0.9 ka, and after which glaciers across the European Alps lost mass as the climate warmed through the Holocene (Ivy-Ochs et al., 2009). Consequently, the starting point for each Holocene simulation was a stable ice configuration that filled the Chamonix Valley at 14 ka, that was spun up over 1,000 years using a mean annual air temperature at sea level of 10.0°C to reach mass balance equilibrium conditions representing climate prior to the start of the Holocene.

The glacier model experiments were forced from this spin-up configuration to the start of the Common Era (0 CE; 2 ka) using a regional Holocene palaeotemperature composite (Temp12k; Kaufman et al., 2020), and then forward through the Common Era to the present day using a glacier change index to represent fluctuations in the extent of the Grosser Aletschgletscher in Switzerland (Holzhauser et al., 2005) calibrated to a present-day mean annual air

https://doi.org/10.5194/egusphere-2026-1536
Preprint. Discussion started: 11 May 2026

temperature of 14.0°C. The Temp12k palaeotemperature forcing is a composite of over 350 calibrated proxy records of median annual air temperature for the latitude band 30–60 °N which has a time step of 500 years (Kaufman et al., 2020). These data give annual air temperature values at sea level that were extrapolated to the model domain using the lapse rate noted above. Total precipitation was fixed throughout the simulation but partitioned between snowfall and rainfall as a function of elevation-dependent air temperature across the model domain. As a result, snow accumulation rates varied seasonally and over time in response to change in air temperatures.

4 Results

4.1 Headwall erosion rates

^{10}Be exposure ages of the four samples from Petit Flambeau give ages with internal uncertainties of between 50 ± 20 years and 80 ± 10 years for the three samples collected close to the glacier surface (n = 3), whereas one sample (MDG-HF-04) collected 200 m above the glacier surface yielded an exposure age of 560 ± 20 years (Fig. 4b and Table 1). Inverse modelling of the TCN results together with the $IRSL_{50}$ RSED results gave average steady-state erosion rates of 0.5 ± 0.6 mm a^{-1} over a period of about 20–200 years for samples near to the glacier surface, while sample MDG-HF-04 gave a steady-state erosion rate of about 0.1 mm a^{-1} averaged over ~30 years (Table 1). The $IRSL_{225}$ signal data yielded similar but slightly lower erosion rates, whilst the OSL_{125} signal data yielded erosion rates of about 0.1 mm a^{-1} for both the lower samples and MDG-HF-04. Maximum erosion rates, integrated over the past year were 1–2 mm a^{-1} for the $IRSL_{50}$ signal, 3–4 mm a^{-1} for the $IRSL_{225}$ signal and 1–2 mm a^{-1} for the OSL_{125} signal. Based on the $IRSL_{50}$ results, we infer that the current erosion rate at the Petit Flambeau headwall is in the range of 0.1–1.0 mm a^{-1} and represents conditions over the last 100 years.

Table 1. ^{10}Be and luminescence RSED apparent ages and erosion rates, obtained using a paired inversion method (Lehmann et al., 2019a,b).
*SS= Steady state

https://doi.org/10.5194/egusphere-2026-1536
Preprint. Discussion started: 11 May 2026

Samples	Cores	Lat [dd]	Long [dd]	Altitude [m.a.s.l]	Shielding correction	^{10}Be conc. [at g_{qtz}^{-1}]	^{10}Be apparent age ± internal error [a]	Luminescence signal	Luminescence surface exposure apparent age [a]	Time t_S at SS* [a]	$\dot{\varepsilon}$ at SS* [mm a^{-1}]	Average $\dot{\varepsilon}$ at SS* [mm a^{-1}]
MDG-HF-01	1	45.84986	6.92798	3219	0.773169	2599±223	80±10	$IRSL_{50}$	1.66±0.13	Out of bounds	*0.001*	**0.38±0.31**
	2							RSL_{50}	191.10±26.76	121.0	0.596	
	1							$IRSL_{225}$	1.60±0.10	79.10	0.339	
	2							$IRSL_{225}$	13.96±1.30	160.0	0.869	
	1							OSL_{125}	1.60±0.13	105.0	0.494	
	2							OSL_{125}	64.65±11.57	Out of bounds	*0.001*	
MDG-HF-02	1	45.85013	6.92820	3219	0.722932	2112±196	70±10	$IRSL_{50}$	60.61±3.53	Out of bounds	*0.001*	**0.04±0.05**
	1							$IRSL_{225}$	11.06±0.51	34.0	0.110	
	1							OSL_{125}	33.61±3.50	9.56	0.020	
MDG-HF-03	1	45.85035	6.92828	3219	0.611187	1388±319	50±20	$IRSL_{50}$	5.11±0.80	51.80	0.193	**0.42±0.53**
	2							$IRSL_{50}$	0.65±0.12	244.0	1.526	
	1							$IRSL_{225}$	16.02±2.04	29.50	0.091	
	2							$IRSL_{225}$	2.44±0.13	121.0	0.560	
	1							OSL_{125}	93.18±24.40	Out of bounds	0.001	
	2							OSL_{125}	6.28±0.64	39.10	0.133	
MDG-HF-04	1	45.85013	6.92811	3416	0.881049	30083±109	560±20	$IRSL_{50}$	5.45±0.80	34.0	0.1099	**0.06±0.04**
	3							$IRSL_{50}$	481.19±34.21	-	-	
	1							$IRSL_{225}$	12.05±1.17	34.0	0.11	
	3							$IRSL_{225}$	21.08±2.26	22.30	0.063	
	1							OSL_{125}	64.05±4.38	4.72	0.008	
	3							OSL_{125}	111.35±8.04	6.26	0.012	

https://doi.org/10.5194/egusphere-2026-1536
Preprint. Discussion started: 11 May 2026

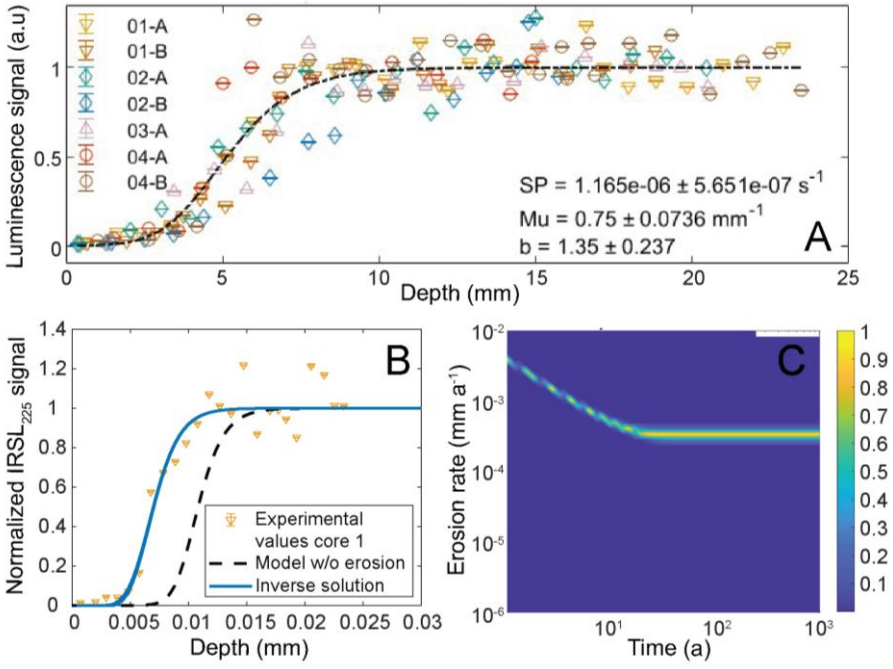

Figure 2. Erosion rates calculated from the headwall of the Mer de Glace. A. Luminescence depth profiles for each core of each calibration sample for the $IRSL_{225}$ signal, fitted with a general-order kinetic model (Freiesleben et al., 2023; Pathan et al., 2024). B. Luminescence depth profile of unknown age sample MDG-HF-01 fitted using the parameters determined in A. C. Erosion rate of sample MDG-HF-01, inverted from the luminescence data in B paired with a ^{10}Be apparent age of 80±10 a (Sample MDG-HF-01). See text for further details.

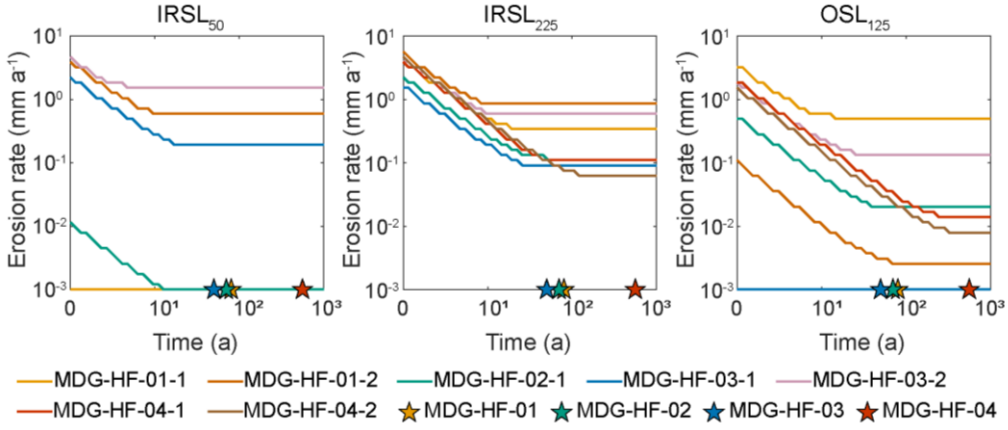

Figure 3. Summary of erosion rates inverted from paired RSED and ^{10}Be data for the different samples. Coloured stars show the ^{10}Be apparent ages for the four headwall samples.

https://doi.org/10.5194/egusphere-2026-1536
Preprint. Discussion started: 11 May 2026

4.2 Englacial clast burial ages

Luminescence signal (L_n/T_n) bleaching plateaus are absent in 30 % of the collected samples which could be explained by a lack of exposure to light on the headwall or that the clasts were produced and transported subglacially before being emplaced close to the glacier surface by thrusting in the ablation area. Alternatively, these clasts could have fractured during rock fall or been abraded during englacial transport to reveal surfaces without prior exposure to light. Half of the dated samples have a short plateau (2-4 adjacent rock fragments) suggesting that these samples were only exposed to light for a comparatively short period of time, consistent with rapid transport on hillslopes and into the glacier.

Of the 27 luminescence RSBD samples measured that passed the dose-recovery test, 15 yielded $IRSL_{50}$ and 4 $IRSL_{225}$ bleaching plateaus comprising >2 rock fragments whilst no OSL_{125} data recovered dose within 10% of unity. Residual ages were estimated following 24 h bleaching in a Hönle UVACube 400 solar simulator and vary between 0.24 ± 0.12 and 3.31 ± 7.54 ka for $IRSL_{50}$ and 0.66 ± 0.08 and 1.21 ± 0.35 ka for $IRSL_{225}$ signals (Table 2), corresponding to ~50 % of the mean ages (Table 2, Fig. 10, S72). However, as residual-uncorrected dose recovery ratios are closer to unity and the chosen laboratory bleaching duration does most likely not reflect the true light exposure conditions of the dated clasts, ages have not been residual-corrected (Supplementary Materials Section 3.5).

The mean fading-corrected ages range from 0.58 ± 0.13 ka to 6.73 ± 0.72 ka for $IRSL_{50}$, and from 1.48 ± 0.5 ka to 5.79 ± 2.37 ka for $IRSL_{225}$. For samples dated with both $IRSL_{50}$ and $IRSL_{225}$, the $IRSL_{225}$ ages are consistently older (Table 2). Significant age differences can be observed between rock fragments of the same core (Supplementary Materials Section 3.5). Cores with longer plateaus (>6 rock fragments) generally yield more consistent ages than cores with shorter plateaus (Figure S44).

Two or more faces were dated for half of the samples and show similar results, with average ages between two cores from the same sample ranging from 0.27 ka to 1.79 ka for $IRSL_{50}$ and from 0.28 to 4.3 ka for $IRSL_{225}$ (Table 2).

Table 2. Luminescence results for each core. In bold are the accepted ages.
[1] Dose rate at the surface (1st slice). [2]$N_{5\%}$ is the number of fragments who pass the 5 % threshold, N_p the number of aliquots dated, N the number of aliquots used to calculate the mean age. [3]For g-values < 1%/decade, no fading correction has been made (Buylaert et al., 2009). [4]Slice number of the rock fragment in the bleaching plateau with the lowest age; if no indication is given, the first slice yields the youngest age (S1 = rock surface).

https://doi.org/10.5194/egusphere-2026-1536
Preprint. Discussion started: 11 May 2026

Cores	Lat [dd]	Long [dd]	Total dose rate ± err [Gy ka^{-1}] s1[1]	Signal	$N_{5\%}$[2]	N_p[2]	N[2]	D_e ± SD [Gy] (lower)	Residual age ± SD [ka]	DRR ± SD [%]	Fading rate [%/decade]	Lower age ± SD [ka] (Corr)[4]	Age ± SD [ka] (Corr)	Mean sample age [ka]
MDG23_01_A2	45.91430	6.93764	5.93±0.32	$IRSL_{50}$	3	3	2	2.93±0.19	0.24±0.12	0.89±0.05	5.55±1.07	0.63±0.08	0.72±0.09	**0.58±0.13**
				$IRSL_{225}$	2	2	1	11.83±2.43	0.66±0.08	0.87±0.09	0.65±0.92[3]	1.99±0.42	1.99±0.42	1.81±0.26
MDG23_01_B1	45.91430	6.93764	6.04±0.33	$IRSL_{50}$	7	7	4	1.74±0.09	0.24±0.12	0.89±0.05	5.55±1.07	0.37±0.04	0.45±0.08	
				$IRSL_{225}$	3	3	2	9.09±1.02	0.66±0.08	0.87±0.09	0.65±0.92[3]	1.51±0.19	1.63±0.13	
MDG23_04_A1	45.91592	6.93581	6.15±0.22	$IRSL_{50}$	7	7	6	2.39±0.15	0.53±0.12	1.08±0.12	4.17±0.66	*0.50±0.05*	0.64±0.08	**0.79±0.15**
				$IRSL_{225}$	5	5	4	16.10±5.1	0.86±0.21	1.07±0.25	1.98±0.18	2.84±0.89	3.14±0.20	2.78±0.36
MDG23_04_B1	45.91592	6.93581	6.34±0.22	$IRSL_{50}$	7	7	6	2.30±0.53	0.53±0.12	1.08±0.12	4.17±0.66	0.48±0.13	0.94±0.10	
				$IRSL_{225}$	4	4	3	14.7±0.9	0.86±0.21	1.07±0.25	1.98±0.18	2.64±0.19	3.42±0.59	
MDG23_06_A1	45.91431	6.93764	5.89±0.31	$IRSL_{50}$	2	2	1	6.74±1.22	0.54±0.04	1.04±0.11	3.01±0.63	1.44±0.29	**1.44±0.29**	
MDG23_07_A1	45.91431	6.93764	6.55±0.34	$IRSL_{50}$	3	3	2	5.49±0.54	0.51±0.07	1.07±0.07	7.27±0.69	1.53±0.23	2.05±0.52	**2.07±0.24**
MDG23_07_C1	45.91431	6.93764	6.21±0.32	$IRSL_{50}$	2	2	2	4.52±0.53	0.51±0.07	1.07±0.07	7.27±0.69	1.32±0.22	1.80±0.47	
MDG23_07_D1	45.91431	6.93764	6.21±0.32	$IRSL_{50}$	4	4	2	6.17±0.86	0.51±0.07	1.07±0.07	7.27±0.69	2.00±0.36	2.38±0.38	
MDG23_08_C1	45.91531	6.93736	5.46±6.84	$IRSL_{50}$	5	5	2	5.01±1.08	0.59±0.33	1.05±0.11	3.19±1.06	*1.02±0.28*	**1.51±0.49**	
MDG23_10_A2	45.92327	6.92472	7.33±0.39	$IRSL_{50}$	4	4	3	1.42±0.38	0.50±0.10	0.92±0.04	5.07±0.29	0.28±0.08	0.95±0.73	**1.22±0.27**
				$IRSL_{225}$	2	2	2	6.15±8.27	0.98±0.16	1.00±0.13	2.10±0.64	0.98±1.02	1.48±0.50	3.64±2.15
MDG23_10_B2	45.92327	6.92472	6.62±0.35	$IRSL_{50}$	4	4	3	4.80±0.62	0.50±0.10	0.92±0.04	5.07±0.29	1.07±0.16	1.50±0.38	
				$IRSL_{225}$	2	2	1	32.2±13.2	0.98±0.16	1.00±0.13	2.10±0.64	5.79±2.37	5.79±2.37	
MDG_01_A	45.92506	6.92304	5.81±0.31	$IRSL_{50}$	6	6	5	2.64±0.43	0.47±0.03	1.04±0.08	3.72±0.25	0.58±0.10	**0.67±0.09**	
MDG_02_B	45.92506	6.92304	6.26±0.34	$IRSL_{50}$	7	7	5	1.59±0.31	0.51±0.06	1.02±0.04	4.58±1.76	*0.33±0.09*	**0.88±0.17**	
MDG_06_A	45.93016	6.92509	1.03±2.35	$IRSL_{50}$	5	3	2	18.54±0.19	3.31±7.54	1.02±0.09	3.99±0.62	6.01±3.49	**6.73±0.72**	
MDG_07_A	45.93008	6.92444	6.92±0.41	$IRSL_{50}$	2	2	2	3.27±0.37	0.51±0.10	0.98±0.06	6.73±1.25	0.79±0.18	**0.85±0.06**	
MDG_09_A	45.92949	6.92429	6.84±0.23	$IRSL_{50}$	5	3	3	2.37±0.51	0.26±0.05	0.85±0.07	7.76±1.40	*0.34±0.07*	4.30±2.6	**6.13±0.42**
MDG_16_A	45.92131	6.92591	6.32±0.32	$IRSL_{50}$	4	4	3	5.28±0.70	0.61±0.18	1.09±0.11	4.75±1.87	1.18±0.33	**1.47±0.37**	
				$IRSL_{225}$	2	2	2	19.52±4.00	0.92±0.26	1.25±0.28	3.60±0.31	4.15±0.9	4.52±0.37	
MDG_19_A	45.92000	6.92641	6.86±0.27	$IRSL_{50}$	2	2	2	2.55±1.15	0.54±0.08	1.17±0.11	4.50±0.89	*0.51±0.24*	**2.27±1.76**	
MDG_20_A	45.92000	6.92641	5.92±0.31	$IRSL_{50}$	9	8	7	1.82±0.22	0.75±0.05	1.02±0.12	2.93±0.23	*0.35±0.05*	0.71±0.39	**1.06±0.90**
MDG_20_B	45.92000	6.92641	5.75±0.30	$IRSL_{50}$	5	5	4	7.35±0.24	0.75±0.05	1.02±0.12	2.93±0.23	1.60±0.11	2.50±1.10	
MDG_33_A	45.92518	6.92299	6.02±0.33	$IRSL_{50}$	3	3	2	1.28±0.24	0.35±0.05	1.03±0.07	9.03±0.13	0.42±0.09	**0.80±0.63**	

400

https://doi.org/10.5194/egusphere-2026-1536
Preprint. Discussion started: 11 May 2026

Samples were collected along the centre of the glacier at several sites at distances of 0.7–2.8 km (± 50 m) from the glacier terminus, and several samples were collected from each site. The dense spatial sampling of englacial clasts at each sampling site allowed multiple burial ages to be obtained per site. The resulting ages are dispersed, clustering between 0.5 ka and 2.3 ka and yielded a mean of 1.2 ka when excluding the two oldest samples (MDG_06 and MDG_09; Fig. 4, Table 2). The youngest ages are consistent across all sampled areas along the glacier. No systematic age trend along the glacier transect was evident; at the terminus, ages ranged from ~0.8 to 6.8 ka, whereas further up glacier the samples exhibit a narrower age range of ~0.8 to 2.3 ka. At the uppermost sampling site, ages varied between 0.58 ± 0.13 ka and 2.07 ± 0.24 ka (Fig. 4).

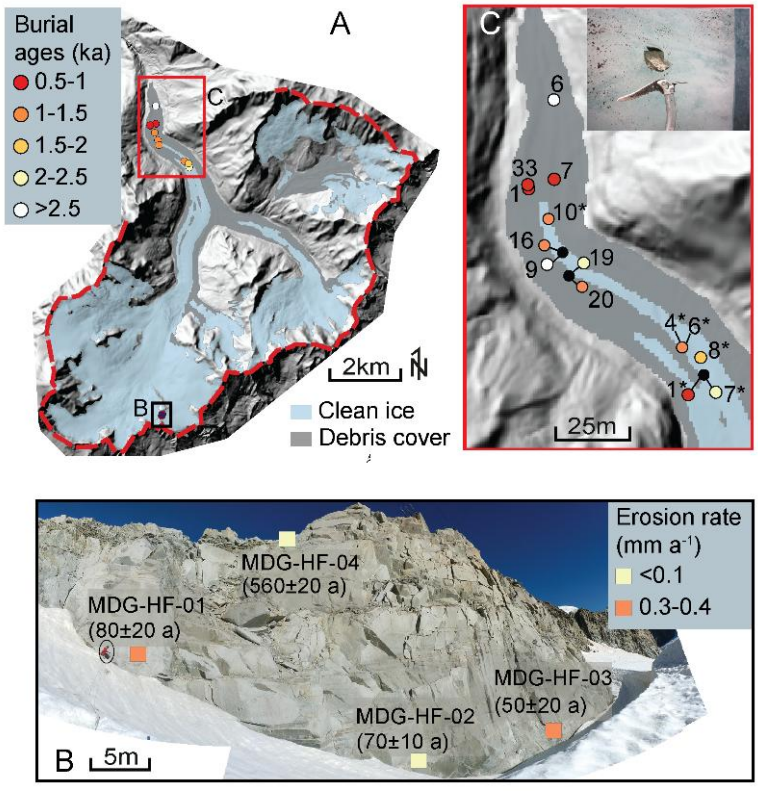

Figure 4. A) Map of the Mer de Glace catchment showing the locations of samples used for headwall erosion rate determination and englacial burial dating. Burial ages are indicated by the colour of the dots. B) Photograph of the headwall site used for erosion rate determinations, showing apparent ^{10}Be exposure ages and inferred erosion rates. A person is highlighted for scale. C) Zoom on the lower part of the ablation area highlighting the burial ages. For clarity, sample numbers are shown without the MDG prefix. Asterisks (*) indicate samples collected in 2023.

https://doi.org/10.5194/egusphere-2026-1536
Preprint. Discussion started: 11 May 2026

4.3 Glacier modelling results

4.3.1 Evaluation of the present-day simulation

The simulations of Mer de Glace were compared with present-day observations of glacier velocity (Lliboutry and Reynaud, 1981; Millan et al., 2022) and estimated ice thickness (Farinotti et al., 2019; Millan et al. 2022) to determine the optimal simulation that best represented the present-day glacier and the evolution of this glacier through the Holocene. The optimal simulation (Fig. 5) used the mass balance parameterisation and forcing described in Section 3.4 and a headwall erosion rate of 1.0 mm a^{-1}, in agreement with our measurements of headwall erosion rates at the Petit Flambeau and erosion rates of headwalls determined for other glacial catchments in the Mont Blanc massif (Lehmann et al., 2019b; Sarr et al., 2019). The simulated extent of Mer de Glace was similar to that indicated by geomorphic evidence from lateral and terminal moraines representing the LIA extent of the glacier (Fig. 7C).

In the optimal simulation, the spatial distribution of ice thickness was similar to the estimated results, although the maximum simulated ice thickness of 277 m (Fig. 5A) was somewhat lower than the estimated values of 331 m from Farinotti et al. (2019) and 459 m from Millan et al. (2022) (Fig. 5B–D). Simulated ice flow reached a maximum of 160 m a^{-1} in the Séracs du Géant icefall (Fig. 5E) and was consistent with field measurements of annual surface velocity for Mer de Glace of 120–210 m a^{-1} between 1964 and 1979 CE (Lliboutry & Reynaud, 1981) and are also comparable with ice flow values simulated in a previous study of Mer de Glace (Peyaud et al., 2020). The global velocity dataset (Fig. 5F and 5G) gave values of up to 800 m a^{-1} in the Séracs du Géant icefall (Millan et al., 2022) and overestimates both ice thickness and velocity for Mer de Glace when compared with observations and our simulations. This is a common problem when using estimated global data products for individual glaciers (Pritchard et al., 2026) that in part results from the filtering of such datasets to remove low values which are beyond the resolution of the method used to produce these data products.

4.3.2 Impact of headwall erosion rate on the evolution of Mer de Glace

The impact on glacier changes through the Holocene of differing headwall erosion rates of 1.0 mm a^{-1}, 5.0 mm a^{-1} and 10 mm a^{-1} was tested to encompass the range of values derived from paired ^{10}Be and luminescence measurements at the Petit Flambeau headwall (Fig. 6). The erosion rate was held constant through each simulation,

https://doi.org/10.5194/egusphere-2026-1536
Preprint. Discussion started: 11 May 2026

with the volume of sediment production limited by the availability of hillslopes that exceeded the critical thickness for erosion and sediment transport, such that sediment production by hillslope erosion varied spatially and temporally. The production of sediment was therefore topographically controlled, with the total hillslope lowering during the Holocene under the highest erosion rate of 75 m on the steepest slopes, with a mean hillslope lowering value of 6.1 m across the entire catchment. Some areas of the catchment increased rather than decreased in elevation by up to 12.2 m during the same period due to the accumulation of sediment. In the simulation with the higher erosion rate, the difference in elevation of the topographic surface across the model domain (specifically on the headwalls in the accumulation area) was 17 m lower than in the simulation with the lower erosion rate. The change in glacier mass/volume through the Holocene simulation resulting from an order of magnitude change in erosion rate was insignificant (Fig. 6C).

The impact of the accumulation of debris produced by erosion on mass balance and glacier evolution was tested and found to have a negligible effect on the evolution of Mer de Glace, because the area covered by supraglacial debris represented only a small fraction of the ablation area of this glacier through the Holocene, and as such the impact on net glacier mass balance of the insulation by supraglacial debris was small (Fig. 6D–F). The impact on Holocene glacier change of an order of magnitude change in headwall erosion rate was minor because; (1) the majority of erosion and sediment production occurred during deglaciation, representing the flux of sediment resulting from destabilisation of hillslopes following glacier recession, and the resulting change in topography of the catchment had little effect on ELA, and (2) supraglacial debris accumulation at Mer de Glace was minimal, such that a reduction in ablation to account for insulation of the ice surface by supraglacial debris resulted in only a slightly more extensive glacier (Fig. 6D–F).

https://doi.org/10.5194/egusphere-2026-1536
Preprint. Discussion started: 11 May 2026

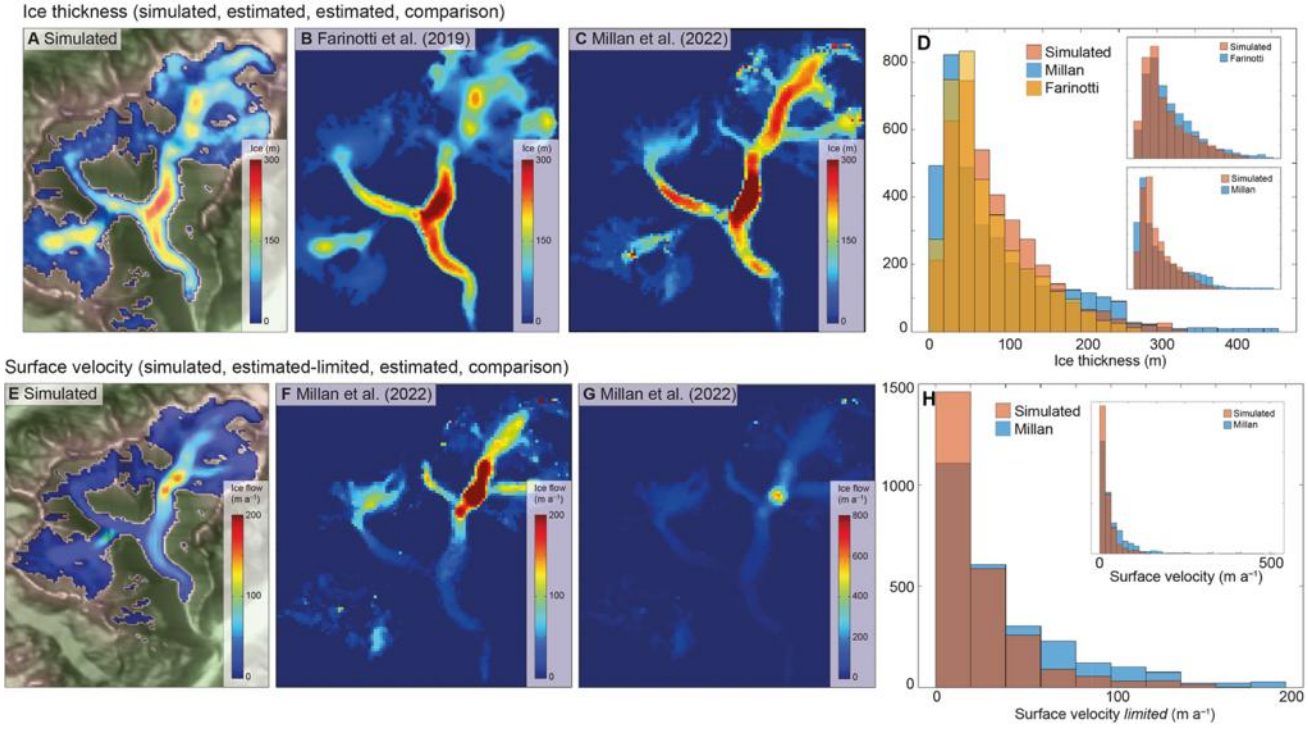

Figure 5. Glacier model sensitivity experiment results for evaluation of present-day simulation showing (a–d) simulated ice thickness compared with estimated ice thickness for Mer de Glace from Farinotti et al. (2019) and Millan et al. (2022), (e–h) simulated glacier surface velocity (displacement) compared with observed surface velocity from Millan et al. (2022), shown on the same colourbar scale (0–200 m a^{-1}) and with a more complete scale for displacement (0–800 m a^{-1}). Note that the maximum values in the Millan et al. (2022) dataset are up to 800 m a^{-1} but only occur in a small number of cells.

https://doi.org/10.5194/egusphere-2026-1536
Preprint. Discussion started: 11 May 2026

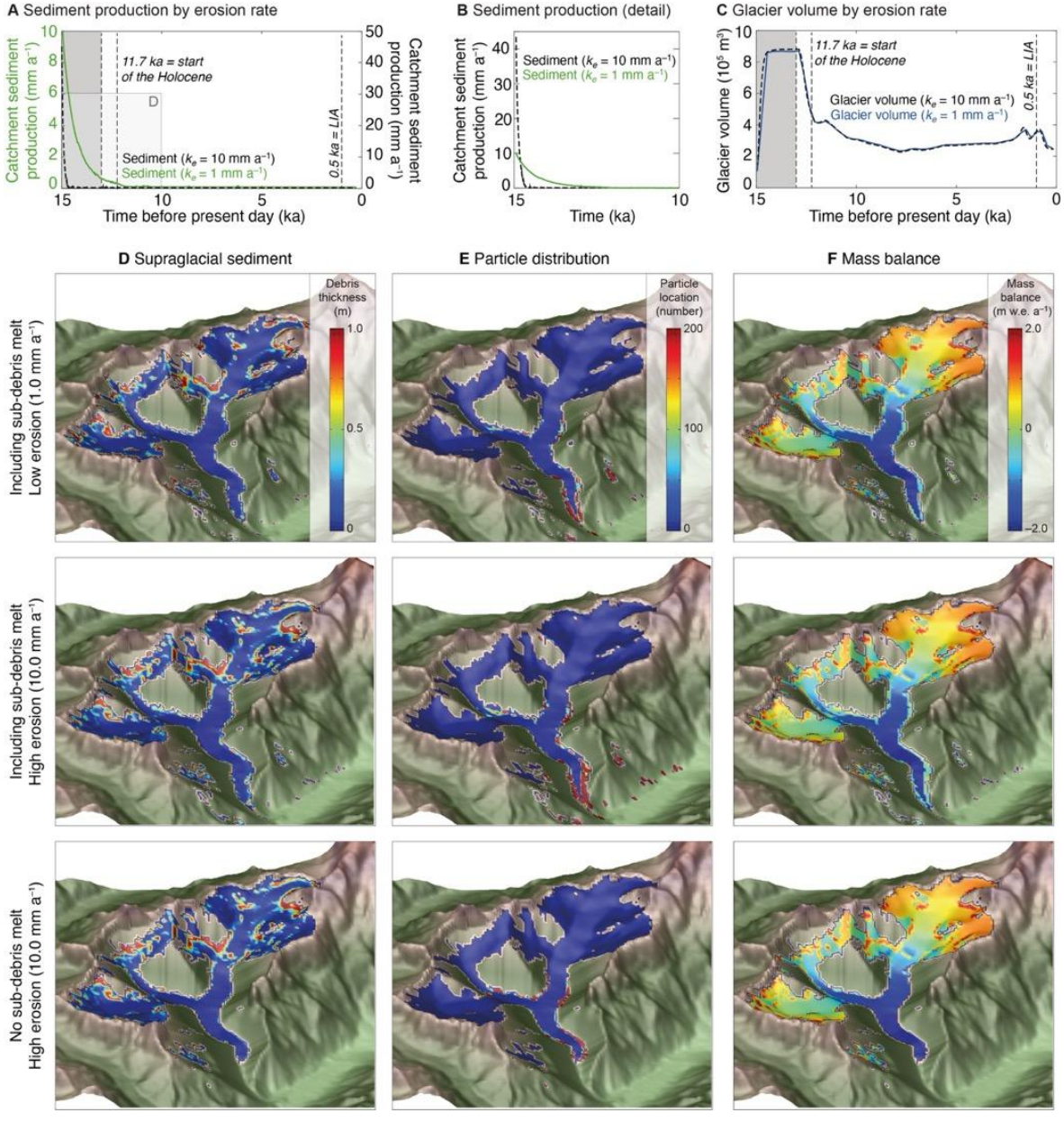

Figure 6. Results from three experiments showing the impact of sub-debris melt and headwall erosion rate on the evolution of Mer de Glace showing (A) Catchment sediment production from headwall erosion over time as a function of headwall erosion rate (k_e) with values for k_e of 10.0 mm a^{-1} and 1.0 mm a^{-1}, (B) detail of 15–10 ka in (A), (C) glacier volume change over time as a result of different values for k_e and the results for the present-day glacier configuration with two different erosion rates and with and without sub-debris melt for the high erosion rate showing (D) simulated supraglacial sediment distribution, (E) the location of sediment in englacial transport (distribution of particles) and (F) the glacier mass balance showing the impact of snow avalanching on accumulation and supraglacial debris on ablation in each case.

https://doi.org/10.5194/egusphere-2026-1536
Preprint. Discussion started: 11 May 2026

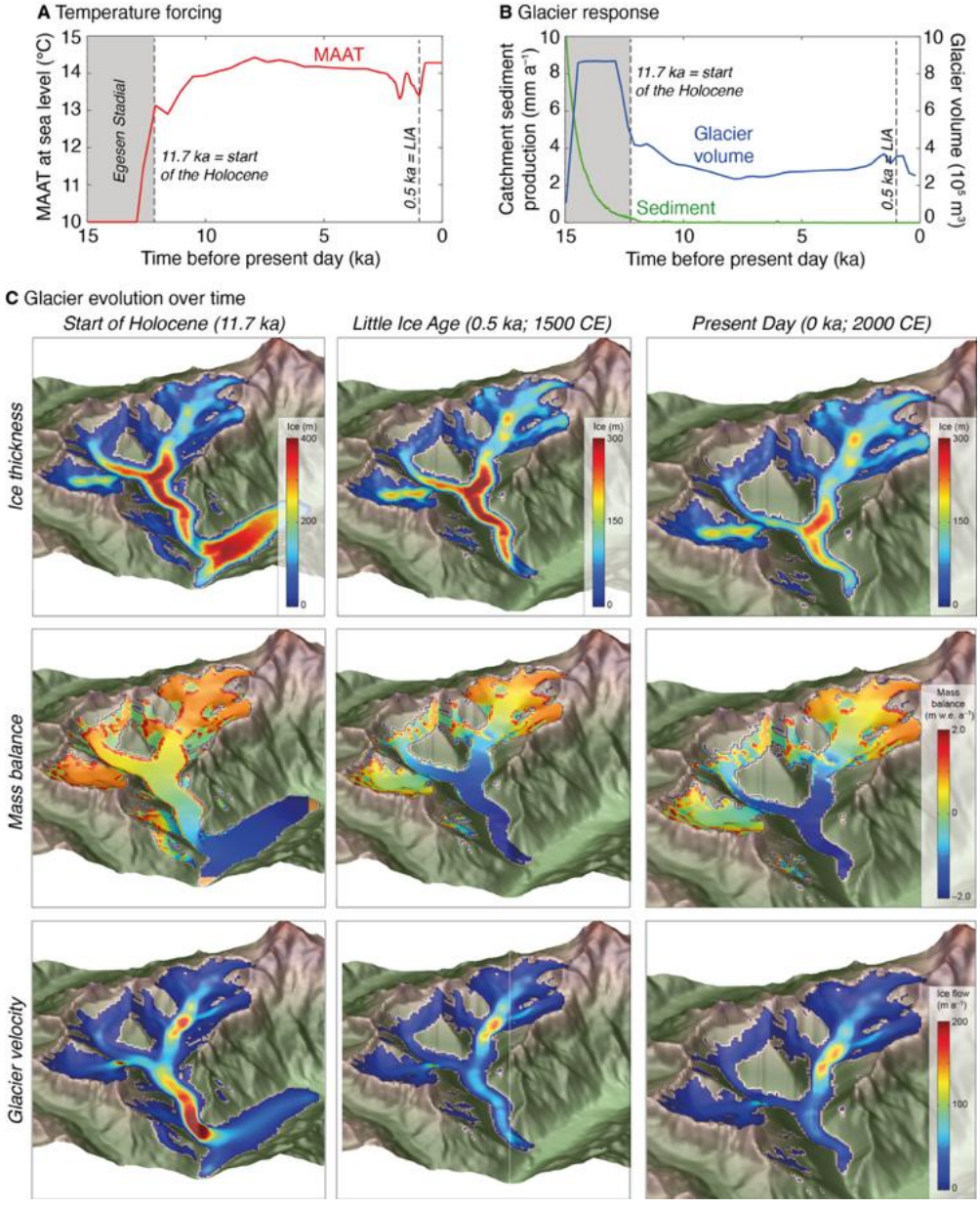

Figure 7. Glacier model forcing and results from the optimal simulation, showing (A) mean annual air temperature forcing for the Holocene from the Temp12k dataset, (B) simulated catchment-wide sediment production, and (C) simulated glacier volume change through the Holocene. The map-view figures show simulated ice thickness, mass balance and glacier velocity for the start of the Holocene, the LIA maximum (~1500 CE), and the present day (2000 CE) glacier. In the mass balance panel for the start of the Holocene, the imposed margins of the ice mass in the Chamonix Valley are shaded brown. Note that the colour scale for ice thickness differs between the panels and is shown for each figure.

https://doi.org/10.5194/egusphere-2026-1536
Preprint. Discussion started: 11 May 2026

4.3.2 Simulated sediment transport times through the Mer de Glace catchment

The glacier model simulated 657 englacial particle trajectories greater than 1 km in length, of which 548 trajectories (83%) represented sediment transport that remained within the uppermost 10% of the ice column (Fig. 8B). Multiple particles travelled along each of these trajectories, such that these represent established englacial sediment flowpaths. The mean englacial sediment transport time was 803 years from the time the particle was entrained within the ice to the time the particle was deposited onto a moraine at the ice margin (Fig. 8A). However, this value does not represent the positively skewed distribution of sediment transport times across the Holocene simulation that results from the pathways by which sediment is transported through Mer de Glace; in the simulated glacier, 80% of particle trajectories represented sediment transport in the upper ice column or at the glacier surface and have transport durations of less than 500 years, while the remaining 20% of particle transport durations are much longer, representing sediment transport at depth in the glacier and deposition of sediment in moraines and on hillslopes before being re-entrained into glacial transport, resulting in sediment transport durations of up to 1,000 years at the lateral ice margins in the accumulation areas of Mer de Glace (Fig. 8). The typical duration of sediment transport through Mer de Glace is in the order of hundreds of years for sediment transported the entire length of the glacier (11.5 km from the headwall to the terminus) rather than sediment that remains stored in the accumulation area and travels less than 6 km in englacial transport (Fig. 9).

https://doi.org/10.5194/egusphere-2026-1536
Preprint. Discussion started: 11 May 2026

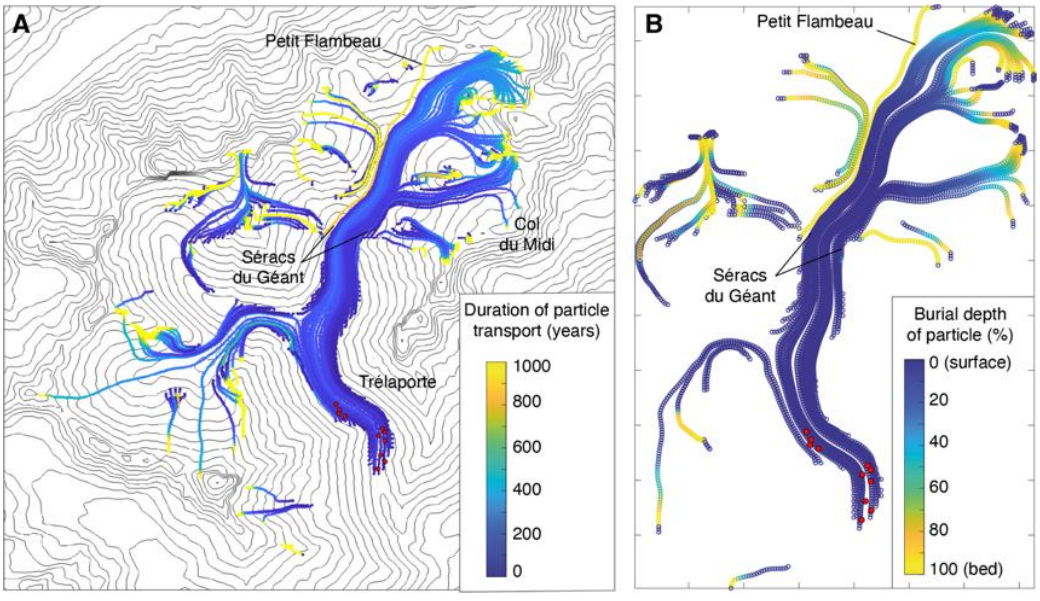

Figure 8. Simulated particle transport time and depth through Mer de Glace. (A) Particle trajectories showing the time in transport for particles at the present day, i.e., the time before the present day that is required to move the particle to the current position at the end of the trajectory flowline. (B) The same particle trajectories showing the depth at which the particle is found within the ice at each point along the flowline. Red dots show the location of the samples collected for luminescence measurements.

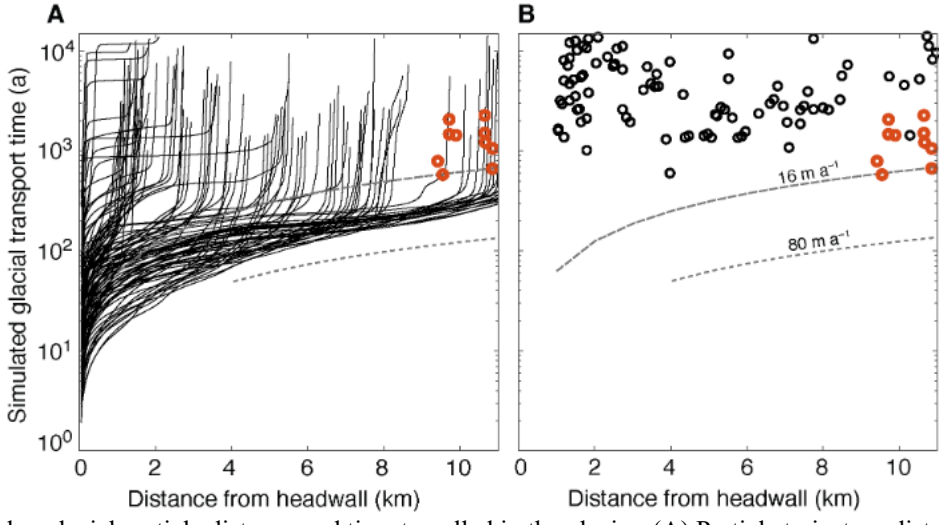

Figure 9. Simulated englacial particle distance and time travelled in the glacier. (A) Particle trajectory distance plotted against time for each of the 657 simulated sediment transport flowlines. (B) The location in time and distance of sediment particles in the present day. Black lines/points showing simulated particle trajectories and locations, and the red dots show the sample locations and ages derived from luminescence RSBD measurements. The grey dashed lines show the cumulative clast transport time estimated using two different glacier surface velocity values (16 m a^{-1} and 80 m a^{-1}). Note the log scale for transport time and linear scale for transport distance from the headwall where the particle first entered glacial transport.

https://doi.org/10.5194/egusphere-2026-1536
Preprint. Discussion started: 11 May 2026

5 Discussion

5.1 Erosion rates estimated from TCN and luminescence rock surface exposure dating

Combined luminescence RSED and TCN dating show that the recently deglaciated Petit Flambeau headwall has experienced erosion rates of 0.1–5 mm a^{-1} over the last 10–100 years. These values are consistent with those reported in recent studies from the Mont Blanc massif. For example, Lehmann et al. (2019b) estimated erosion rates between 3.5 ± 1.2 × 10^{-3} mm a^{-1} and 4.3 ± 0.6 mm a^{-1} on rock surfaces on the hillslopes surrounding the ablation area of Mer de Glace (2000–2500 m a.s.l.) over timescales of 10^2–10^4 years using a similar approach, and found that erosion rates were higher at lower elevations close to the glacier surface. Courtial-Manent et al. (2025) quantified erosion rates on the major headwall above our sampling site, reporting pre-20th-Century values using ^{10}Be ranging from 0.2–2.2 mm a^{-1} and present-day rates exceeding 4.1 mm a^{-1} from terrestrial laser scanning of the headwall between 2006 and 2011. The erosion rates obtained by Lehmann et al. (2019b) and Courtial-Manent et al. (2025) align well with those we obtain in the upper part of our catchment near the glacier surface. However, the values reported by Lehmann et al. (2019b) may slightly overestimate erosion because their luminescence data were fitted using a first-order kinetic model, which is generally a poor description of the behaviour feldspar luminescence data. The RSED data in this study were calculated following the approach of Freiesleben et al. (2023a and 2023b) and Pathan et al. (2024), using a general-order kinetic model (McKeever & Chen, 1997).

Guillon et al. (2015) estimated periglacial erosion rates of 0.29 ± 0.17 mm a^{-1} for the Bossons Glacier catchment in the Mont Blanc massif using ^{10}Be from supraglacial sediments. In the same catchment, Sarr et al. (2019) constrained headwall retreat rates also using ^{10}Be, obtaining rates of 0.19 ± 0.08 mm a^{-1}, 0.54 ± 0.10 mm a^{-1}, and 1.08 ± 0.17 mm a^{-1} across distinct rockfall zones in the Bossons catchment, yielding a mean periglacial erosion rate of 0.65 mm a^{-1}. Although ^{10}Be integrates erosion rates over longer timescales than luminescence measurements, these ^{10}Be-derived erosion rates are consistent with our short-term erosion rate estimates. These comparisons indicate that our combined luminescence–cosmogenic dating approach has constrained erosion rates that are coherent with independent short- and long-term estimates (ranging from 3.5 × 10^{-3} mm a^{-1} to 5 mm a^{-1}) over about 100 years, and from 0.19 mm a^{-1} to 2.2 mm a^{-1} over 100-1000 year timescales for steep, recently deglaciated headwalls in the Mont Blanc massif. Our short-term estimates (< 10^2 years) likely primarily reflect surface weathering, whereas the long-term estimates capture erosion associated with rockfalls (e.g. Lehmann et al.,

https://doi.org/10.5194/egusphere-2026-1536
Preprint. Discussion started: 11 May 2026

2019b; Sarr et al., 2019). The headwall erosion rates are likely controlled by a combination of climatic effects such as frost cracking and morphometric factors including the local structure of the bedrock and the occurrence of preexisting fractures (e.g., Scherler, 2014; Lehmann et al., 2019b).

5.2 Sediment transport, storage and provenance in the Mer de Glace catchment

The RSBD luminescence ages obtained along the Mer de Glace reflect the burial duration of englacial clasts within the glacier. The multiple ages obtained in individual locations allow comparison of sediment transport and storage processes recorded by the clast luminescence ages. These ages cluster at 0.8 ka, 1.5 ka, 2.2 ka and 6.7 ka for a total of 15 rock surface burial ages (Fig. 10A, B). Different ages were obtained from the same area of the glacier, which could result from factors including temporary storage of sediment in cold ice aprons, hanging glaciers, or ice-marginal moraines, and differences in provenance (i.e. clasts sourced from different tributary glacier catchments) or from transport at different depths within the ice column. The Mer de Glace catchment has a complex geometry with five tributary glaciers, and the combination of tributary glaciers with different elevations and geometries results in slightly different mass balance gradients and causes unsynchronised variation in ice flow and debris flux into the main glacier tongue (Rowan et al., 2015; Kirkbride et al., 2023). However, the simulation of particle trajectories through Mer de Glace suggests that the sediment locations sampled contain ice that originated from the Geant Glacier catchment (Fig. 8B).

The younger sample ages (~0.8 ka) are broadly consistent across each location and align with the simulated particle ages and estimates of transport time in the upper ice column from feature-tracking and field observations of glacier surface velocity along the central flowline (Fig. 9). The observed glacier surface velocity of 50–80 m a^{-1} measured in the 1970s (Lliboutry and Reynaud, 1981) in the lower ablation area immediately up glacier of the sampling area would imply an age difference of 100–160 years along the 2 km sampling transect. Luminescence RSBD cannot resolve such small age differences and the clasts dated have a greater minimum age for each area. We therefore consider the younger age population to represent broadly continuous englacial transport between the time that the sediment was entrained into the glacier in the Glacier du Géant accumulation area and the time that the sediment was sampled from the lower ablation area.

In contrast, the older sample ages (1.5 ka, 2.2 ka, 6.7 ka) represent a more complex sediment transport history and appear to correspond to known warm intervals during the Holocene (Fig. 10). The oldest age (6.7 ka) corresponds

https://doi.org/10.5194/egusphere-2026-1536
Preprint. Discussion started: 11 May 2026

to the mid-Holocene climatic optimum during which period glaciers in the Mont Blanc massif and Swiss Alps reached their minimum extents (e.g., Hormes et al., 2001; Joerin et al., 2006; Orombelli, 2011); and some alpine summits experienced ice-free conditions (e.g., Hafner, 2012; Bohleber et al., 2020). The sample ages of 2.5 ka and 1.2 ka correspond to the Roman Warm Period when warmer conditions were experienced in Europe and glaciers were generally smaller than at present (e.g., Hormes et al., 2001; Goehring et al., 2012). We propose that the older ages we obtain record long-term storage of sediments in the upper part of the MDG catchment during periods of reduced glacier extent. As climate cooled again, this material was slowly remobilised and transported by the glacier. The difference ranging from 0.27 ka to 1.79 ka in $IRSL_{50}$ ages between faces of the same clasts (MDG23-01 between core A2 and core B1 and MDG-20 core A and B, table 2) further supports successive burial phases with intermittent bleaching, consistent with remobilisation of previously stored material.

These warm intervals in the Holocene coincide with periods of enhanced rockfall activity on the headwalls of Glacier du Géant, where two clusters of high rockfall activity were dated using ^{10}Be to the mid-Holocene (8.2–4.2 ka) and the Roman Warm Period (~2 ka) (Bohleber et al., 2020; Gallach et al., 2018). More recent periods of high rockfall activity have also been observed in this catchment (<0.56 ka; Bohleber et al., 2020; Gallach et al., 2018) and at Miage Glacier (post-LIA; Stewart et al., 2025) that have resulted in the recent expansion of supraglacial debris and could explain a greater frequency of younger clasts sampled from Mer de Glace. The luminescence samples from the debris-covered areas of Mer de Glace show more scattered ages and shorter plateaus, reflecting faster erosion rates and limited exposure times on the headwalls, which supports sediment input from rockfalls rather than subglacial quarrying.

5.3 Sediment storage times in glacierised catchments and implications for landscape evolution

Englacial sediment storage and transport times were constrained for two glaciers in the Mont Blanc massif in the European Alps—Mer de Glace and Miage Glacier (Margirier et al., 2025; this study). The two catchments differ markedly in terms of the geometry and accumulation area extent of their glaciers and the provenance and magnitude of sediment supply from their headwalls. Despite these contrasts, luminescence burial ages from Mer de Glace and Miage Glacier are broadly comparable (Fig. 10). The samples from Miage Glacier yielded ages ranging from 0 ± 0.1 to 4.7 ± 0.3 ka (n = 7), while those from Mer de Glace ranged from 0.58 ± 0.13 to 6.73 ± 0.72 ka (n = 15). The sampled clasts from Mer de Glace display longer bleaching plateaus than those from Miage Glacier, likely

https://doi.org/10.5194/egusphere-2026-1536
Preprint. Discussion started: 11 May 2026

reflecting the contrasting lithologies or headwall erosion rates between the two catchments rather than differences in transport processes. For both glaciers, the younger ages (<1 ka) are interpreted as representing englacial transport durations that directly reflect the rate of ice flow through the glacier, whereas older ages (>1 ka) indicate long durations of sediment storage at the ice margins or within moraines prior to re-entrainment and additional glacial transport. Approximately 40% of clasts from Miage Glacier and 70% from Mer de Glace record burial durations exceeding 1 ka, demonstrating that long-term sediment storage occurs even in steep, actively eroding, alpine glacial catchments. Ages older than 1 ka from both catchments coincide with warmer phases of the Holocene inferred from lake-sediment temperature reconstructions (Fig. 10B, C; Kaufman et al., 2020). These ages also align with the chronology of archaeological artefacts recovered at Schnidejoch Pass, which document periods when the pass was ice-free and accessible for human crossing (Fig. 10D; Hafner, 2012; Hafner & Schwörer, 2018). These results suggest that sediment accumulation and storage in the upper parts of glaciated catchments of the Mont Blanc Massif were favoured during warmer phases and intervals of reduced glacier extent. Such periods likely also corresponded to enhanced sediment production, particularly through increased rockfall activity on headwalls (e.g., Bohleber et al., 2020; Gallach et al., 2018). Subsequent climatic cooling would have promoted glacier expansion, leading to the progressive remobilization and englacial transport of previously stored sediment. The observed storage durations highlight the capacity of glacierised catchments to store and release sediments during fluctuations in glacier extent in response to climate change, which will modulate sediment delivery downstream over millennial timescales. This interpretation expands from the theoretical model of paraglacial sediment flux over time following deglaciation of Church & Ryder (1972), who proposed that only alluvial fans and valley-fill deposits acted as transient sediment storage and ultimately routed sediment downstream, despite these landforms typically being more stable than glacierised catchments. In contrast, our results show that the glacierised parts of mountain catchments can store sediment over millennial timescales rather than being solely locations of sediment transfer or only very short-lived deposition (Church & Ryder, 1972). Our results demonstrate that sediments can persist in a glaciated catchment for millennia, with younger ages reflecting transport within the ice and older ages reflecting combined transport in the ice and temporary sediment storage.

The multiple clusters of burial age durations suggest a complex interplay between glacier dynamics, sediment transport and storage, and Holocene climate variability (Fig. 10). Our results imply that millennial-scale residence times within glacierised catchments introduce a time lag between erosion in headwalls and the deposition of sediments in proximal sedimentary sinks. Temporary sediment storage in high-alpine valleys has been documented

https://doi.org/10.5194/egusphere-2026-1536
Preprint. Discussion started: 11 May 2026

in various deposits, including moraines, proglacial plains, glacial lakes, debris cones, and alluvial terraces (e.g., in the Turtmann Valley in the Swiss Alps; Otto et al., (2009)). Sediment provenance studies further emphasise the importance of moraines and other reworked glacial deposits as sediment sources in glaciated catchments (van Woerkom et al., 2019). Moraine materials reflect sediment derived from a broad range of elevations, whereas modern river sediments appear to originate almost exclusively from the erosion of ice-exposed moraines, suggesting that elevated sediment flux during deglaciation is largely driven by the remobilisation of unconsolidated moraine deposits rather than increased bedrock erosion (Jess et al., 2025). However, moraine composition may also mirror that of stored subglacial sediment, and the relative contribution of subglacial sediment production and storage may increase during deglaciation and with increasing annual precipitation (Norris et al., 2025; Delaney et al., 2026).

Storage and lag time associated with glacierised catchments add to those associated with sediment storage in piedmonts, alluvial plains, and lacustrine or coastal environments, influencing the temporal accuracy of erosional, provenance and climatic signals in sedimentary archives (Phillips & Slattery, 2006; Blöthe & Korup, 2013; Clift & Giosan, 2014; Romans et al., 2016; Malatesta et al., 2018). Previously glaciated, high-elevation floodplains in the Colorado Front Range exhibit sediment residence times on the order of 10^2–10^3 years (Sutfin & Wohl, 2019). In larger mountain systems such as the Himalaya, mean residence times between ~3 ka and 32 ka have been reported, with over 85% of total sediment volumes stored upstream of major syntaxes (Blöthe & Korup, 2013). Although Alpine catchments are smaller, our results suggest that sediment storage in the upper parts of glacierized systems is not negligible compared to other storage domains and likely exerts a control on sediment export and stratigraphic completeness in downstream records. In lower-elevation catchments, soil-mantled hillslopes can store sediment for >200 ka and constitute the dominant storage domain, as shown in the Var River basin (Southern French Alps; Thollon et al., 2023). However, they generate comparatively little sediment, in contrast to glacierized catchments where sediment production is substantially higher.

https://doi.org/10.5194/egusphere-2026-1536
Preprint. Discussion started: 11 May 2026

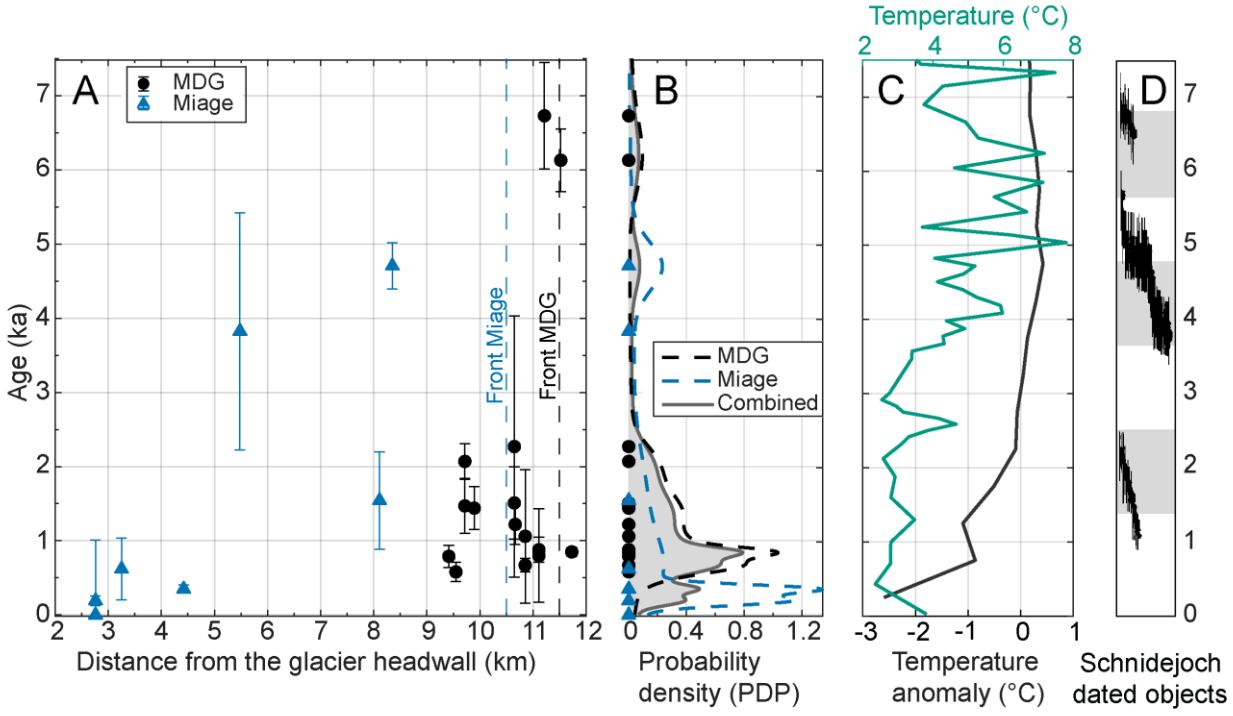

Figure 10. Comparison of burial ages from the Mer de Glace and Miage glaciers with Holocene climate indicators. A) Burial ages from the Mer de Glace and Miage glaciers plotted against modelled travel distance from the glacier headwall. Glacier front positions are from the GLIMS database (GLIMS Consortium, 2005). B) Probability density (PDP) estimates of burial ages from the two glaciers. C) Holocene palaeotemperatures. Temp12K composite temperature anomaly based on more than 350 calibrated proxy records of median annual air temperature for the 30–60 °N latitude band, used as input for glacier modelling in this study (black curve; see section 3.4.4.). Temperature composite derived from the warmest and coldest months reconstructed from the sediment of Grächen See, Switzerland (green curve) (Kaufman et al., 2020). D) Calibrated radiocarbon dates of archaeological findings at Schnidejoch shown as probability distributions (modified from Hafner & Schwörer, 2018). Grey bars indicate periods of increased solar activity, corresponding to Hallstatt cycle maxima at ~6.2, ~4.5, ~2 ka, and the present (Nussbaumer et al., 2011).

6. Conclusions

The dataset of englacial clast burial ages derived using luminescence rock surface burial dating presented here provides new constraints on both sediment transport timescales and sediment storage during the Holocene within the deglaciating Mer de Glace catchment. Our results indicate that englacial sediment transport generally occurs over sub-millennial timescales (< 1 ka), but that a significant proportion of clasts record burial durations of 1.5 ka, 2.2 ka, and up to 6.7 ka indicating significant periods of sediment storage at the ice margins prior to further transport. These geochronological results are supported by glacier modelling, which indicates that while 80% of

https://doi.org/10.5194/egusphere-2026-1536
Preprint. Discussion started: 11 May 2026

clasts are continuously transported in the upper part of the ice column and deposited from the glacier within a few hundred years of entrainment, 20% of clasts have a more complex transport history through the Mer de Glace catchment and represent sediment in transport through the glacierised section of the catchment for thousands of years. Results for Mer de Glace and Miage Glacier in the Mont Blanc massif demonstrate that sediment can remain within Alpine glacier systems for several millennia before being released beyond the limit of glaciation and into fluvial systems. Such extended residence times highlight the capacity of glacierised catchments to temporarily store material even under dynamic ice-flow conditions. This millennial-scale buffering has important implications for interpreting the timing of sediment transport over glacial-interglacial cycles and the formation of sedimentary archives during periods of Quaternary climate change, as these results identify significant temporal lags between the erosion, transport, and deposition of sediment, which have the potential to obscuring short-term climatic signals even in proximal depositional environments.

Code and data availability

The source code for the iSOSIA model (spm-3.4.8) and a test simulation for Miage Glacier are available from Zenodo (Rowan & Pedersen, 2024; https://zenodo.org/records/10959201).

^{10}Be sample information has been added to the ICE-D version 2 database to allow data access and recalibration (https://version2.ice-d.org/alpine/site/Petit%20Flambeau/; Site 7569).

The luminescence measurements of the englacial rocks and headwall bedrock samples are available in Zenodo (Rodari et al., 2026; https://doi.org/10.5281/zenodo.19081855). The MATLAB and R codes used for luminescence rock surface burial dating are also provided with the dataset in Zenodo (Rodari et al., 2026).

Sample availability

Prepared quartz used for ^{10}Be measurements of each sample is available for appropriate re-use where there is sufficient material remaining, after discussion with the corresponding author.

Supplement link: the link to the supplement will be included by Copernicus, if applicable.

https://doi.org/10.5194/egusphere-2026-1536
Preprint. Discussion started: 11 May 2026

Author contribution:

Conceptualisation: G.E. King, A.V. Rowan

Data curation: L. Rodari

Formal analysis: L. Rodari, A. Margirier, A.V. Rowan, G.E. King

Funding acquisition: G.E. King, A.V. Rowan

Investigation: L. Rodari, A. Margirier, A.V. Rowan, G.E. King, C. Schmidt, D. Fabel, G. Jouvet

Methodology: L. Rodari, A. Margirier, A.V. Rowan, G.E. King

Project administration: G.E. King

Resources: G.E. King, C. Schmidt, A. V. Rowan, D. Fabel

Supervision: G.E. King, A.V. Rowan, A. Margirier

Validation: L. Rodari, A. Margirier, A.V. Rowan, G.E. King

Visualisation: L. Rodari, A. Margirier, A.V. Rowan, G.E. King

Writing (original draft preparation): L. Rodari, A.V. Rowan, A. Margirier, G.E. King

Writing (review and editing): L. Rodari, A.V. Rowan, G.E. King, A. Margirier, C. Schmidt, V. Pedersen, C.S. Curry, A.C. Scoffield, C.R. Diemont, R. Veness, G. Jouvet, D. Fabel

Fieldwork: L. Rodari, A. Margirier, R. Veness, A.V. Rowan, G.E. King, C.S. Curry, A.C. Scoffield, C.R. Diemont, F. Perchanok

Competing interests

The authors declare that they have no conflict of interest.

Acknowledgements: We thank B. Lehmann and A.N. Pathan for sharing the codes used to determine erosion rates, and S. Cook and B. Finley for useful discussion. Thanks to K. Diba, M. Godenzi and N. Pontiggia for their support for the luminescence samples preparation.

Financial support:

Fieldwork at Mer de Glace in 2021 was supported by a Royal Society Dorothy Hodgkin Research Fellowship (DHF\R1\201113) to AVR. The glacier model simulations presented were performed using resources provided by Sigma2, the National Infrastructure for High-Performance Computing and Data Storage in Norway.

https://doi.org/10.5194/egusphere-2026-1536
Preprint. Discussion started: 11 May 2026

References

Alley, R. B., Cuffey, K. M., Evenson, E. B., Strasser, J. C., Lawson, D. E., & Larson, G. J. (1997). How glaciers entrain and transport basal sediment: Physical constraints. *Quaternary Science Reviews*, *16*(9), 1017–1038. https://doi.org/10.1016/S0277-3791(97)00034-6

Anderson, R. S. (2000). A model of ablation-dominated medial moraines and the generation of debris-mantled glacier snouts. *Journal of Glaciology*, *46*(154), 459–469. https://doi.org/10.3189/172756500781833025

Anderson, R. S., Dühnforth, M., Colgan, W., & Anderson, L. (2012). Far-flung moraines: Exploring the feedback of glacial erosion on the evolution of glacier length. *Geomorphology*, *179*, 269–285. https://doi.org/10.1016/j.geomorph.2012.08.018

Auclair, M., Lamothe, M., & Huot, S. (2003). Measurement of anomalous fading for feldspar IRSL using SAR. *Radiation Measurements, Proceedings of the 10th International Conference on Luminescence and Electron-Spin Resonance Dating (LED 2002)*, *37*(4), 487–492. https://doi.org/10.1016/S1350-4487(03)00018-0

Balescu, S., & Lamothe, M. (1994). Comparison of TL and IRSL age estimates of feldspar coarse grains from waterlain sediments. *Quaternary Science Reviews*, *13*(5–7), 437–444. https://doi.org/10.1016/0277-3791(94)90056-6

Bell, W. T. (1979). Attenuation factors for the absorbed radiation in quartz inclusions for thermoluminescence dating. *Ancient TL*, *3*(3), 2–13. https://doi.org/10.26034/la.atl.1979.022

Bernard, M., Steer, P., Gallagher, K., & Lundbek Egholm, D. (2020). Modelling the effects of ice transport and sediment sources on the form of detrital thermochronological age probability distributions from glacial settings. *Earth Surface Dynamics*, *8*(4), 931–953. https://doi.org/10.5194/esurf-8-931-2020

Berthier, E., Arnaud, Y., Baratoux, D., Vincent, C., & Rémy, F. (2004). Recent rapid thinning of the "Mer de Glace" glacier derived from satellite optical images. *Geophysical Research Letters*, *31*(17). https://doi.org/10.1029/2004GL020706

Berthier, E., & Vincent, C. (2012). Relative contribution of surface mass-balance and ice-flux changes to the accelerated thinning of Mer de Glace, French Alps, over1979-2008. *Journal of Glaciology*, *58*(209), 501–512. https://doi.org/10.3189/2012JoG11J083

Biswas, R. H., Pathan, A. N., & Malik, J. N. (2023). General order kinetics model for OSL rock surface exposure dating. *Proceedings of the Indian National Science Academy*, *89*(3), 644–654. https://doi.org/10.1007/s43538-023-00172-y

Blöthe, J. H., & Korup, O. (2013). Millennial lag times in the Himalayan sediment routing system. *Earth and Planetary Science Letters*, *382*, 38–46. https://doi.org/10.1016/j.epsl.2013.08.044

Bohleber, P., Schwikowski, M., Stocker-Waldhuber, M., Fang, L., & Fischer, A. (2020). New glacier evidence for ice-free summits during the life of the Tyrolean Iceman. *Scientific Reports*, *10*(1), 20513. https://doi.org/10.1038/s41598-020-77518-9

Brennan, B. J., Lyons, R. G., & Phillips, S. W. (1991). Attenuation of alpha particle track dose for spherical grains. *International Journal of Radiation Applications and Instrumentation. Part D. Nuclear Tracks and Radiation Measurements*, *18*(1), 249–253. https://doi.org/10.1016/1359-0189(91)90119-3

Bundesamt für Landestopografie swisstopo; Tarquini S., I. Isola, M. Favalli, A. Battistini, G. Dotta (2023). TINITALY, a digital elevation model of Italy with a 10 meters cell size (Version 1.1). Istituto Nazionale di Geofisica e Vulcanologia (INGV). https://doi.org/10.13127/tinitaly/1.1; DGM Österreich, geoland.at; DGM1, Bayerische Vermessungsverwaltung – www.geodaten.bayern.de; DGM1, Baden-Württemberg: LGL, www.lgl-bw.de, dl-de/by-2-0"; RGEAlti, Institut National de l'information géographique et forestière, données originales téléchargées sur https://geoservices.ign.fr/rgealti#telechargement5m, mise à jour du juillet 2023

Buylaert, J. P., Murray, A. S., Thomsen, K. J., & Jain, M. (2009). Testing the potential of an elevated temperature IRSL signal from K-feldspar. *Radiation Measurements, Proceedings of the 12th International Conference on Luminescence and Electron Spin Resonance Dating (LED 2008)*, *44*(5), 560–565. https://doi.org/10.1016/j.radmeas.2009.02.007

Church, M., & Ryder, J. M. (1972). Paraglacial Sedimentation: A Consideration of Fluvial Processes Conditioned by Glaciation. *GSA Bulletin*, *83*(10), 3059–3072. https://doi.org/10.1130/0016-7606(1972)83%255B3059:PSACOF%255D2.0.CO;2

https://doi.org/10.5194/egusphere-2026-1536
Preprint. Discussion started: 11 May 2026

Claude, A., Ivy-Ochs, S., Kober, F., Antognini, M., Salcher, B., & Kubik, P. W. (2014). The Chironico landslide (Valle Leventina, southern Swiss Alps): Age and evolution. *Swiss Journal of Geosciences*, *107*(2), 273–291. https://doi.org/10.1007/s00015-014-0170-z

Clift, P. D., & Giosan, L. (2014). Sediment fluxes and buffering in the post-glacial Indus Basin. *Basin Research*, *26*(3), 369–386. https://doi.org/10.1111/bre.12038

Courtial-Manent, L., Mugnier, J.-L., Ravanel, L., Carcaillet, J., Deline, P., & Buoncristiani, J.-F. (2025). A significant doubling of rockfall rates since the Little Ice Age in the Mont-Blanc massif, inferred from 10Be concentrations and rockfall inventories. *Earth and Planetary Science Letters*, *651*, 119142. https://doi.org/10.1016/j.epsl.2024.119142

Delaney, I., Margirier, A., Gevers, M., Jenkin, M., Leger, T., Vergara, I., Seguinot, J., Jouvet, G., Aitken, A. R. A., Lane, S. N., Herman, F., & King, G. E. (2026). Increased glacier melt enhances erosion and sediment export across timescales. *JGR, Earth Surface*.

Deline, P. (2005). Change in surface debris cover on Mont Blanc massif glaciers after the'Little Ice Age' termination. *The Holocene*, *15*(2), 302–309. https://doi.org/10.1191/0959683605hl809rr

Deline, P. (2009). Interactions between rock avalanches and glaciers in the Mont Blanc massif during the late Holocene. *Quaternary Science Reviews, Natural Hazards, Extreme Events and Mountain Topography*, *28*(11), 1070–1083. https://doi.org/10.1016/j.quascirev.2008.09.025

Deline, P., Gruber, S., Delaloye, R., Fischer, L., Geertsema, M., Giardino, M., Hasler, A., Kirkbride, M., Krautblatter, M., Magnin, F., McColl, S., Ravanel, L., & Schoeneich, P. (2015). Ice Loss and Slope Stability in High-Mountain Regions. In *Snow and Ice-Related Hazards, Risks, and Disasters* (pp. 521–561). Academic Press. https://doi.org/10.1016/B978-0-12-394849-6.00015-9

Durcan, J. A., King, G. E., & Duller, G. A. T. (2015). DRAC: Dose Rate and Age Calculator for trapped charge dating. *Quaternary Geochronology*, *28*, 54–61. https://doi.org/10.1016/j.quageo.2015.03.012

Egholm, D. L., Knudsen, M. F., Clark, C. D., & Lesemann, J. E. (2011). Modeling the flow of glaciers in steep terrains: The integrated second-order shallow ice approximation (iSOSIA). *Journal of Geophysical Research: Earth Surface*, *116*(F2). https://doi.org/10.1029/2010JF001900

Elkadi, J., King, G. E., Lehmann, B., & Herman, F. (2021). Reducing variability in OSL rock surface dating profiles. *Quaternary Geochronology*, *64*, 101169. https://doi.org/10.1016/j.quageo.2021.101169

Farinotti, D., Huss, M., Fürst, J. J., Landmann, J., Machguth, H., Maussion, F., & Pandit, A. (2019). A consensus estimate for the ice thickness distribution of all glaciers on Earth. *Nature Geoscience*, *12*(3), 168–173. https://doi.org/10.1038/s41561-019-0300-3

Freiesleben, T. H., Thomsen, K. J., & Jain, M. (2023). Novel luminescence kinetic models for rock surface exposure dating. *Radiation Measurements*, *160*, 106877. https://doi.org/10.1016/j.radmeas.2022.106877

Freiesleben, T. H., Thomsen, K. J., Sellwood, E., Liu, J., & Murray, A. S. (2023). Testing new kinetic models and calibration methods for Rock Surface Luminescence Exposure dating using controlled experiments. *Radiation Measurements*, *169*, 107033. https://doi.org/10.1016/j.radmeas.2023.107033

Freiesleben, T., Sohbati, R., Murray, A., Jain, M., al Khasawneh, S., Hvidt, S., & Jakobsen, B. (2015). Mathematical model quantifies multiple daylight exposure and burial events for rock surfaces using luminescence dating. *Radiation Measurements, 14th International Conference on Luminescence and Electron Spin Resonance Dating, 7–11 July, 2014, Montréal, Canada*, *81*, 16–22. https://doi.org/10.1016/j.radmeas.2015.02.004

Fyffe, C. L., Woodget, A. S., Kirkbride, M. P., Deline, P., Westoby, M. J., & Brock, B. W. (2020). Processes at the margins of supraglacial debris cover: Quantifying dirty ice ablation and debris redistribution. *Earth Surface Processes and Landforms*, *45*(10), 2272–2290. https://doi.org/10.1002/esp.4879

Gallach, X., Ravanel, L., Egli, M., Brandova, D., Schaepman, M., Christl, M., Gruber, S., Deline, P., Carcaillet, J., & Pallandre, F. (2018). Timing of rockfalls in the Mont Blanc massif (Western Alps): Evidence from surface exposure dating with cosmogenic 10Be. *Landslides*, *15*(10), 1991–2000. https://doi.org/10.1007/s10346-018-0999-8

GLACIOCLIM. (2019). [Data set]. https://glacioclim.osug.fr/Mer-de-Glace-125

GLIMS Consortium. (2005). *GLIMS Glacier Database, Version 1* [Data set]. National Snow and Ice Data Center. https://doi.org/10.7265/N5V98602

https://doi.org/10.5194/egusphere-2026-1536
Preprint. Discussion started: 11 May 2026

Goehring, B. M., Vacco, D. A., Alley, R. B., & Schaefer, J. M. (2012). Holocene dynamics of the Rhone Glacier, Switzerland, deduced from ice flow models and cosmogenic nuclides. *Earth and Planetary Science Letters*, *351–352*, 27–35. https://doi.org/10.1016/j.epsl.2012.07.027

Goodsell, B., Hambrey, M. J., & Glasser, N. F. (2005). Debris transport in a temperate valley glacier: Haut Glacier d'Arolla, Valais, Switzerland. *Journal of Glaciology*, *51*(172), 139–146. https://doi.org/10.3189/172756505781829647

Guérin, G., Mercier, N., & Adamiec, G. (2011). Dose rate conversion factors: Update. *Ancient TL*, *29*(1), 5–8. https://www.aber.ac.uk/en/media/departmental/dges/ancienttl/pdf/vol29no1/atl-issue29-1.pdf#page=9

Guillon, H., Mugnier, J.-L., Buoncristiani, J.-F., Carcaillet, J., Godon, C., Prud'homme, C., van der Beek, P., & Vassallo, R. (2015). Improved discrimination of subglacial and periglacial erosion using 10Be concentration measurements in subglacial and supraglacial sediment load of the Bossons glacier (Mont Blanc massif, France). *Earth Surface Processes and Landforms*, *40*(9), 1202–1215. https://doi.org/10.1002/esp.3713

Hafner, A. (2012). Archaeological Discoveries on Schnidejoch and at Other Ice Sites in the European Alps. *Arctic*, *65*, 189–202. https://www.jstor.org/stable/41638618

Hafner, A., & Schwörer, C. (2018). Vertical mobility around the high-alpine Schnidejoch Pass. Indications of Neolithic and Bronze Age pastoralism in the Swiss Alps from paleoecological and archaeological sources. *Quaternary International, Casting a Glance over the Mountain – Multi-Proxy Approaches to the Understanding of Vertical Mobility*, *484*, 3–18. https://doi.org/10.1016/j.quaint.2016.12.049

Hallet, B., Hunter, L., & Bogen, J. (1996). Rates of erosion and sediment evacuation by glaciers: A review of field data and their implications. *Global and Planetary Change, Impact of Glaciations on Basin Evolution: Data and Models from the Norwegian Margin and Adjacent Areas*, *12*(1), 213–235. https://doi.org/10.1016/0921-8181(95)00021-6

Hambrey, M. J., Bennett, M. R., Dowdeswell, J. A., Glasser, N. F., & Huddart, D. (1999). Debris entrainment and transfer in polythermal valley glaciers. *Journal of Glaciology*, *45*(149), 69–86. https://doi.org/10.3189/S0022143000003051

Herreid, S., & Pellicciotti, F. (2020). The state of rock debris covering Earth's glaciers. *Nature Geoscience*, *13*(9), 621–627. https://doi.org/10.1038/s41561-020-0615-0

Hock, R. (2003). Temperature index melt modelling in mountain areas. *Journal of Hydrology, Mountain Hydrology and Water Resources*, *282*(1), 104–115. https://doi.org/10.1016/S0022-1694(03)00257-9

Holzhauser, H., Magny, M., & Zumbuühl, H. J. (2005). Glacier and lake-level variations in west-central Europe over the last 3500 years. *The Holocene*, *15*(6), 789–801. https://doi.org/10.1191/0959683605hl853ra

Hormes, A., Müller, B. U., & Schlüchter, C. (2001). The Alps with little ice: Evidence for eight Holocene phases of reduced glacier extent in the Central Swiss Alps. *The Holocene*, *11*(3), 255–265. https://doi.org/10.1191/095968301675275728

Huntley, D. J., & Baril, M. R. (1997). The K content of the K-feldspars being measured in optical dating or in thermoluminesence dating. *Ancient TL*, *15*(1), 11–13.

Iverson, N. R. (1993). Regelation of ice through debris at glacier beds: Implications for sediment transport. *Geology*, *21*(6), 559–562. https://doi.org/10.1130/0091-7613(1993)021%253C0559:ROITDA%253E2.3.CO;2

Ivy-Ochs, S., Kerschner, H., Maisch, M., Christl, M., Kubik, P. W., & Schlüchter, C. (2009). Latest Pleistocene and Holocene glacier variations in the European Alps. *Quaternary Science Reviews, Holocene and Latest Pleistocene Alpine Glacier Fluctuations: A Global Perspective*, *28*(21), 2137–2149. https://doi.org/10.1016/j.quascirev.2009.03.009

Jenkins, G. T. H., Duller, G. A. T., Roberts, H. M., Chiverrell, R. C., & Glasser, N. F. (2018). A new approach for luminescence dating glaciofluvial deposits—High precision optical dating of cobbles. *Quaternary Science Reviews*, *192*, 263–273. https://doi.org/10.1016/j.quascirev.2018.05.036

Jennings, S. J. A., & Hambrey, M. J. (2021). Structures and Deformation in Glaciers and Ice Sheets. *Reviews of Geophysics*, *59*(3), e2021RG000743. https://doi.org/10.1029/2021RG000743

Jess, S., Schoenbohm, L., & Enkelmann, E. (2025). Novel apatite provenance analysis reveals erosion of moraines as primary sediment source during glacial retreat. *Earth and Planetary Science Letters*, *668*, 119560. https://doi.org/10.1016/j.epsl.2025.119560

Joerin, U. E., Stocker, T. F., & Schlüchter, C. (2006). Multicentury glacier fluctuations in the Swiss Alps during the Holocene. *The Holocene*, *16*(5), 697–704. https://doi.org/10.1191/0959683606hl964rp

https://doi.org/10.5194/egusphere-2026-1536
Preprint. Discussion started: 11 May 2026

Jouvet, G., & Funk, M. (2014). Modelling the trajectory of the corpses of mountaineers who disappeared in 1926 on Aletschgletscher, Switzerland. *Journal of Glaciology*, *60*(220), 255–261. https://doi.org/10.3189/2014JoG13J156

Jouvet, G., Röllin, S., Sahli, H., Corcho, J., Gnägi, L., Compagno, L., Sidler, D., Schwikowski, M., Bauder, A., & Funk, M. (2020). Mapping the age of ice of Gauligletscher combining surface radionuclide contamination and ice flow modeling. *The Cryosphere*, *14*(11), 4233–4251. https://doi.org/10.5194/tc-14-4233-2020

Kaufman, D., McKay, N., Routson, C., Erb, M., Davis, B., Heiri, O., Jaccard, S., Tierney, J., Dätwyler, C., Axford, Y., Brussel, T., Cartapanis, O., Chase, B., Dawson, A., de Vernal, A., Engels, S., Jonkers, L., Marsicek, J., Moffa-Sánchez, P., … Zhilich, S. (2020). A global database of Holocene paleotemperature records. *Scientific Data*, *7*(1), 115. https://doi.org/10.1038/s41597-020-0445-3

King, G. E., Valla, P. G., & Lehmann, B. (2019). Rock surface burial and exposure dating. In *Handbook of Luminescence Dating* (pp. 350–372).

Kirkbride, M. P. (2002). Processes of glacial transportation. In *Modern and Past Glacial Environments* (pp. 147–169). Butterworth-Heinemann. https://doi.org/10.1016/B978-075064226-2/50009-X

Kirkbride, M. P., & Deline, P. (2013). The formation of supraglacial debris covers by primary dispersal from transverse englacial debris bands. *Earth Surface Processes and Landforms*, *38*(15), 1779–1792. https://doi.org/10.1002/esp.3416

Kirkbride, M. P., Sherriff, S. C., Rowan, A. V., Egholm, D. L., Quincey, D. J., Miles, E., Hubbard, B., & Miles, K. (2023). Provenance and transport of supraglacial debris revealed by variations in debris geochemistry on Khumbu Glacier, Nepal Himalaya. *Earth Surface Processes and Landforms*, *48*(14), 2737–2753. https://doi.org/10.1002/esp.5657

Korte, M., Donadini, F., & Constable, C. G. (2009). Geomagnetic field for 0–3 ka: 2. A new series of time-varying global models. *Geochemistry, Geophysics, Geosystems*, *10*(6). https://doi.org/10.1029/2008GC002297

Kreutzer, S., Burow, C., Dietze, M., Fuchs, M. C., Fischer, M., & Schmidt, C. (2017). Software in the context of luminescence dating: Status, concepts and suggestions exemplified by the R package `Luminescence'. *Ancient TL*, *35*(2), 1–11.

Kreutzer, S., Schmidt, C., Fuchs, M. C., Dietze, M., Fischer, M., & Fuchs, M. (2012). Introducing an R package for luminescence dating analysis. *Ancient TL*, *30*, 1–8.

Laj, C., Kissel, C., & Beer, J. (2004). High resolution global paleointensity stack since 75 kyr (GLOPIS-75) calibrated to absolute values. *Geophysical Monograph Series*, *145*, 255–265.

Lal, D. (1991). Cosmic ray labeling of erosion surfaces: *In situ* nuclide production rates and erosion models. *Earth and Planetary Science Letters*, *104*(2), 424–439. https://doi.org/10.1016/0012-821X(91)90220-C

Lane, S. N., Bakker, M., Gabbud, C., Micheletti, N., & Saugy, J.-N. (2017). Sediment export, transient landscape response and catchment-scale connectivity following rapid climate warming and Alpine glacier recession. *Geomorphology, Connectivity in Geomorphology from Binghamton 2016*, *277*, 210–227. https://doi.org/10.1016/j.geomorph.2016.02.015

Lappe, T., Kook, M., Murray, A. S., Thomsen, K. J., Buylaert, J. P., & Jain, M. (2015). A new luminescence detection and stimulation head for the Risø TL/OSL reader. *Radiation Measurements*, *81*, 178–184. https://doi.org/10.1016/j.radmeas.2015.02.001

Lehmann, B., Herman, F., Valla, P. G., King, G. E., & Biswas, R. H. (2019a). Evaluating post-glacial bedrock erosion and surface exposure duration by coupling in situ optically stimulated luminescence and ^{10}Be dating. *Earth Surface Dynamics*, *7*(3), 633–662. https://doi.org/10.5194/esurf-7-633-2019

Lehmann, B., Herman, F., Valla, P. G., King, G. E., Biswas, R. H., Ivy-Ochs, S., Steinemann, O., & Christl, M. (2019b). Postglacial erosion of bedrock surfaces and deglaciation timing: New insights from the Mont Blanc massif (western Alps). *Geology*, *48*(2), 139–144. https://doi.org/10.1130/G46585.1

Lehmann, B., Valla, P. G., King, G. E., & Herman, F. (2018). Investigation of OSL surface exposure dating to reconstruct post-LIA glacier fluctuations in the French Alps (Mer de Glace, Mont Blanc massif). *Quaternary Geochronology*, *44*, 63–74. https://doi.org/10.1016/j.quageo.2017.12.002

Lifton, N., Sato, T., & Dunai, T. J. (2014). Scaling *in situ* cosmogenic nuclide production rates using analytical approximations to atmospheric cosmic-ray fluxes. *Earth and Planetary Science Letters*, *386*, 149–160. https://doi.org/10.1016/j.epsl.2013.10.052

https://doi.org/10.5194/egusphere-2026-1536
Preprint. Discussion started: 11 May 2026

Lifton, N., Smart, D. F., & Shea, M. A. (2008). Scaling time-integrated in situ cosmogenic nuclide production rates using a continuous geomagnetic model. *Earth and Planetary Science Letters*, *268*(1), 190–201. https://doi.org/10.1016/j.epsl.2008.01.021

Lliboutry, L., & Reynaud, L. (1981). "Global Dynamics" of a Temperate Valley Glacier, Mer De Glace, and Past Velocities Deduced from Forbes' Bands. *Journal of Glaciology*, *27*(96), 207–226. https://doi.org/10.3189/S0022143000015367

Lüthi, M. P. (2014). Little Ice Age climate reconstruction from ensemble reanalysis of Alpine glacier fluctuations. *The Cryosphere*, *8*(2), 639–650. https://doi.org/10.5194/tc-8-639-2014

Malatesta, L. C., Avouac, J.-P., Brown, N. D., Breitenbach, S. F. M., Pan, J., Chevalier, M.-L., Rhodes, E., Saint-Carlier, D., Zhang, W., Charreau, J., Lavé, J., & Blard, P.-H. (2018). Lag and mixing during sediment transfer across the Tian Shan piedmont caused by climate-driven aggradation–incision cycles. *Basin Research*, *30*(4), 613–635. https://doi.org/10.1111/bre.12267

Margirier, A., Brondex, J., Rowan, A. V., Schmidt, C., Pedersen, V. K., Lehmann, B., Anderson, L. S., Veness, R., Watson, C. S., Swift, D., & King, G. E. (2025). Tracking Sediment Transport Through Miage Glacier, Italy, Using a Lagrangian Approach With Luminescence Rock Surface Burial Dating of Englacial Clasts. *Journal of Geophysical Research: Earth Surface*, *130*(3), e2024JF007773. https://doi.org/10.1029/2024JF007773

Martin, L. C. P., Blard, P.-H., Balco, G., Lavé, J., Delunel, R., Lifton, N., & Laurent, V. (2017). The CREp program and the ICE-D production rate calibration database: A fully parameterizable and updated online tool to compute cosmic-ray exposure ages. *Quaternary Geochronology*, *38*, 25–49. https://doi.org/10.1016/j.quageo.2016.11.006

McKeever, S. W. S., & Chen, R. (1997). Luminescence models. *Radiation Measurements*, *27*(5), 625–661. https://doi.org/10.1016/S1350-4487(97)00203-5

Millan, R., Mouginot, J., Rabatel, A., & Morlighem, M. (2022). Ice velocity and thickness of the world's glaciers. *Nature Geoscience*, *15*(2), 124–129. https://doi.org/10.1038/s41561-021-00885-z

Murray, A. S., & Wintle, A. G. (2000). Luminescence dating of quartz using an improved single-aliquot regenerative-dose protocol. *Radiation Measurements*, *32*(1), 57–73. https://doi.org/10.1016/S1350-4487(99)00253-X

Nicholson, L., Wirbel, A., Mayer, C., & Lambrecht, A. (2021). The Challenge of Non-Stationary Feedbacks in Modeling the Response of Debris-Covered Glaciers to Climate Forcing. *Frontiers in Earth Science*, *9*. https://doi.org/10.3389/feart.2021.662695

Norris, S. L., Gosse, J. C., Millan, R., Mouginot, J., Rabatel, A., Morlighem, M., Bolton, M. S. M., & Alley, R. B. (2025). Drivers of global glacial erosion rates. *Nature Geoscience*, *18*(8), 732–739. https://doi.org/10.1038/s41561-025-01747-8

Nussbaumer, S. U., Steinhilber, F., Trachsel, M., Breitenmoser, P., Beer, J., Blass, A., Grosjean, M., Hafner, A., Holzhauser, H., Wanner, H., & Zumbühl, H. J. (2011). Alpine climate during the Holocene: A comparison between records of glaciers, lake sediments and solar activity. *Journal of Quaternary Science*, *26*(7), 703–713. https://doi.org/10.1002/jqs.1495

Orombelli, G. (2011). Holocene mountain glacier fluctuations: A global overview. *Geografia Fisica e Dinamica Quaternaria*, *34*(1), 17–24. https://doi.org/10.4461/GFDQ.2011.34.2

Otto, J.-C., Schrott, L., Jaboyedoff, M., & Dikau, R. (2009). Quantifying sediment storage in a high alpine valley (Turtmanntal, Switzerland). *Earth Surface Processes and Landforms*, *34*(13), 1726–1742. https://doi.org/10.1002/esp.1856

Pathan, A. N., Biswas, R. H., Lehmann, B., King, G. E., & Herman, F. (2024). Towards accurate modelling of rock surface exposure dating using luminescence to estimate post-exposure erosion rate. *Quaternary Geochronology*, *85*, 101634. https://doi.org/10.1016/j.quageo.2024.101634

Peyaud, V., Bouchayer, C., Gagliardini, O., Vincent, C., Gillet-Chaulet, F., Six, D., & Laarman, O. (2020). Numerical modeling of the dynamics of the Mer de Glace glacier, French Alps: Comparison with past observations and forecasting of near-future evolution. *The Cryosphere*, *14*(11), 3979–3994. https://doi.org/10.5194/tc-14-3979-2020

Phillips, J. D., & Slattery, M. C. (2006). Sediment storage, sea level, and sediment delivery to the ocean by coastal plain rivers. *Progress in Physical Geography: Earth and Environment*, *30*(4), 513–530. https://doi.org/10.1191/0309133306pp494ra

https://doi.org/10.5194/egusphere-2026-1536
Preprint. Discussion started: 11 May 2026

Pritchard, H. D., King, E. C., Goodger, D. J., Boyle, D., Goldberg, D. N., Recinos, B., Orr, A., & Regmi, D. (2026). Towards Bedmap Himalayas: A new airborne glacier thickness survey in Khumbu Himal, Nepal. *Earth System Science Data*, *18*(1), 199–217. https://doi.org/10.5194/essd-18-199-2026

Rades, E. F., Sohbati, R., Lüthgens, C., Jain, M., & Murray, A. S. (2018). First luminescence-depth profiles from boulders from moraine deposits: Insights into glaciation chronology and transport dynamics in Malta valley, Austria. *Radiation Measurements, 15th International Conference on Luminescence and Electron Spin Resonance Dating, 11-15 September 2017*, *120*, 281–289. https://doi.org/10.1016/j.radmeas.2018.08.011

Reid, H. F. (1902). *Mer de Glace Glacier: From the Glacier Photograph Collection.* Boulder, Colorado USA: National Snow and Ice Data Center. Digital media.

Richards, M. (1992). *Luminescence dating of quartzite from the Diring Yuriakh site*. https://summit.sfu.ca/_flysystem/fedora/sfu_migrate/5088/b1487913x.pdf

Riedesel, S., & Autzen, M. (2020). Beta and gamma dose rate attenuation in rocks and sediment. *Radiation Measurements*, *133*, 106295. https://doi.org/10.1016/j.radmeas.2020.106295

Rodari, L., Margirier, A., Schmidt, C., & King, G. (2026). *Luminescence measurements of englacial rocks and headwall bedrock samples from Mer de Glace (French Alps), with associated codes for luminescence rock surface burial dating.* [Data set]. Zenodo. https://doi.org/10.5281/zenodo.19081855

Roering, J. J., Kirchner, J. W., & Dietrich, W. E. (1999). Evidence for nonlinear, diffusive sediment transport on hillslopes and implications for landscape morphology. *Water Resources Research*, *35*(3), 853–870. https://doi.org/10.1029/1998WR900090

Romans, B. W., Castelltort, S., Covault, J. A., Fildani, A., & Walsh, J. P. (2016). Environmental signal propagation in sedimentary systems across timescales. *Earth-Science Reviews, Source-to-Sink Systems: Sediment & Solute Transfer on the Earth Surface*, *153*, 7–29. https://doi.org/10.1016/j.earscirev.2015.07.012

Rowan, A. V., Egholm, D. L., & Clark, C. D. (2022). Forward modelling of the completeness and preservation of palaeoclimate signals recorded by ice-marginal moraines. *Earth Surface Processes and Landforms*, *47*(9), 2198–2208. https://doi.org/10.1002/esp.5371

Rowan, A. V., Egholm, D. L., Quincey, D. J., & Glasser, N. F. (2015). Modelling the feedbacks between mass balance, ice flow and debris transport to predict the response to climate change of debris-covered glaciers in the Himalaya. *Earth and Planetary Science Letters*, *430*, 427–438. https://doi.org/10.1016/j.epsl.2015.09.004

Rowan, A. V., Egholm, D. L., Quincey, D. J., Hubbard, B., King, O., Miles, E. S., Miles, K. E., & Hornsey, J. (2021). The Role of Differential Ablation and Dynamic Detachment in Driving Accelerating Mass Loss From a Debris-Covered Himalayan Glacier. *Journal of Geophysical Research: Earth Surface*, *126*(9), e2020JF005761. https://doi.org/10.1029/2020JF005761

Rowan, A. V., & Pedersen, V. K. (2024). *annvrowan/isosia: iSOSIA version used in Margirier et al.* [Computer software]. Zenodo. https://doi.org/10.5281/zenodo.10959201

Sarr, A.-C., Mugnier, J.-L., Abrahami, R., Carcaillet, J., & Ravanel, L. (2019). Sidewall erosion: Insights from in situ-produced 10Be concentrations measured on supraglacial clasts (Mont Blanc massif, France). *Earth Surface Processes and Landforms*, *44*(10), 1930–1944. https://doi.org/10.1002/esp.4620

Scherler, D. (2014). Climatic limits to headwall retreat in the Khumbu Himalaya, eastern Nepal. *Geology*, *42*(11), 1019–1022. https://doi.org/10.1130/G35975.1

Scherler, D., Bookhagen, B., & Strecker, M. R. (2011). Hillslope-glacier coupling: The interplay of topography and glacial dynamics in High Asia. *Journal of Geophysical Research: Earth Surface*, *116*(F2). https://doi.org/10.1029/2010JF001751

Scherler, D., & Egholm, D. L. (2020). Production and Transport of Supraglacial Debris: Insights From Cosmogenic 10Be and Numerical Modeling, Chhota Shigri Glacier, Indian Himalaya. *Journal of Geophysical Research: Earth Surface*, *125*(10), e2020JF005586. https://doi.org/10.1029/2020JF005586

Sohbati, R., Murray, A. S., Chapot, M. S., Jain, M., & Pederson, J. (2012). Optically stimulated luminescence (OSL) as a chronometer for surface exposure dating. *Journal of Geophysical Research: Solid Earth*, *117*(B9). https://doi.org/10.1029/2012JB009383

https://doi.org/10.5194/egusphere-2026-1536
Preprint. Discussion started: 11 May 2026

Stewart, R., Westoby, M., Dunning, S., Rowan, A. V., & Woodward, J. (2025). Exploring short-term rockfall inventories in deglaciating catchments: From evidencing glacial history to modelling rockfall runout. *Earth Surface Processes and Landforms*, *50*(15), e70217. https://doi.org/10.1002/esp.70217

Sutfin, N. A., & Wohl, E. (2019). Elevational differences in hydrogeomorphic disturbance regime influence sediment residence times within mountain river corridors. *Nature Communications*, *10*(1), 2221. https://doi.org/10.1038/s41467-019-09864-w

Thollon, M., Dosseto, A., Toucanne, S., & Bayon, G. (2023). Controls on sediment residence times in an Alpine river catchment inferred from uranium isotopes. *Earth and Planetary Science Letters*, *611*, 118130. https://doi.org/10.1016/j.epsl.2023.118130

Uppala, S. M., KÅllberg, P. W., Simmons, A. J., Andrae, U., Bechtold, V. D. C., Fiorino, M., Gibson, J. K., Haseler, J., Hernandez, A., Kelly, G. A., Li, X., Onogi, K., Saarinen, S., Sokka, N., Allan, R. P., Andersson, E., Arpe, K., Balmaseda, M. A., Beljaars, A. C. M., … Woollen, J. (2005). The ERA-40 re-analysis. *Quarterly Journal of the Royal Meteorological Society*, *131*(612), 2961–3012. https://doi.org/10.1256/qj.04.176

Vallon, M., Petit, J.-R., & Fabre, B. (1976). Study of an Ice Core to the Bedrock in the Accumulation zone of an Alpine Glacier. *Journal of Glaciology*, *17*(75), 13–28. https://doi.org/10.3189/S0022143000030677

van Woerkom, T., Steiner, J. F., Kraaijenbrink, P. D. A., Miles, E. S., & Immerzeel, W. W. (2019). Sediment supply from lateral moraines to a debris-covered glacier in the Himalaya. *Earth Surface Dynamics*, *7*(2), 411–427. https://doi.org/10.5194/esurf-7-411-2019

Vincent, C. (2010). *L'impact des changements climatiques sur les glaciers alpins* [Theses, Université de Grenoble]. https://theses.hal.science/tel-00596523

Vincent, C., Dumont, M., Six, D., Brun, F., Picard, G., & Arnaud, L. (2018). Why do the dark and light ogives of Forbes bands have similar surface mass balances? *Journal of Glaciology*, *64*(244), 236–246. https://doi.org/10.1017/jog.2018.12

Vincent, C., Harter, M., Gilbert, A., Berthier, E., & Six, D. (2014). Future fluctuations of Mer de Glace, French Alps, assessed using a parameterized model calibrated with past thickness changes. *Annals of Glaciology*, *55*(66), 15–24. https://doi.org/10.3189/2014AoG66A050

Vincent, C., Peyaud, V., Laarman, O., Six, D., Gilbert, A., Gillet-Chaulet, F., Berthier, É., Morin, S., Verfaillie, D., Rabatel, A., Jourdain, B., & Bolibar, J. (2019). Déclin des deux plus grands glaciers des Alpes françaises au cours du XXIe siècle: Argentière et Mer de Glace. *La Météorologie*, *2019*(106), 49–58. https://doi.org/10.4267/2042/70369

von Raumer, J. F., & Bussy, F. (2004). *Mont-Blanc and Aiguilles Rouges—Geology of their polymetamorhic Basement*. *42*. https://serval.unil.ch/resource/serval:BIB_F3C1004512A8.P001/REF.pdf

Wallinga, J., Murray, A., & Wintle, A. (2000). The single-aliquot regenerative-dose (SAR) protocol applied to coarse-grain feldspar. *Radiation Measurements*, *32*(5), 529–533. https://doi.org/10.1016/S1350-4487(00)00091-3

Ziegler, L. B., Constable, C. G., Johnson, C. L., & Tauxe, L. (2011). PADM2M: A penalized maximum likelihood model of the 0–2 Ma palaeomagnetic axial dipole moment. *Geophysical Journal International*, *184*(3), 1069–1089. https://doi.org/10.1111/j.1365-246X.2010.04905.x